Materials Today Bio 32 (2025) 101769

Contents lists available at ScienceDirect

Materials Today Bio

journal homepage: www.journals.elsevier.com/materials-today-bio

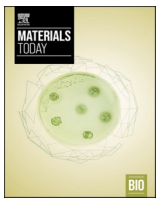

A carbon nanotube/pyrrolidonecarboxylic acid zinc sponge for programmed management of diabetic wounds: Hemostatic, antibacterial, anti-inflammatory, and healing properties

Chenwei Wu [a,1], Bo Liu [b,1], Qiulan Wen [c,1], Qiliang Zhai [a,*]

[a] Department of Urology, Ganzhou Hospital-Nanfang Hospital, Southern Medical University, Ganzhou, Jiangxi, 341000, China
[b] Department of Burns and Plastics Surgery, Liuzhou Worker's Hospital, Fourth Affiliated Hospital of Guangxi Medical University, Liuzhou, Guangxi, 545000, China
[c] Department of Orthopaedic Surgery, Nanfang Hospital, Southern Medical University, Guangzhou, Guangdong Province, 510515, China

ARTICLE INFO

Keywords:
Carbon nanotubes
Zinc pyrrolidone carboxylate
Photothermal conversion
Endogenous electric field
Wound healing

ABSTRACT

Wound healing in patients with diabetes is challenging because of chronic inflammation, inadequate vascularization, and susceptibility to infection. Current wound dressings often target specific stages of healing and lack comprehensive therapeutic approaches. This study introduces a novel approach using a photodetachable sponge scaffold incorporating carbon nanotubes (CNTs), known for their high photothermal conversion efficiency, electrical conductivity, and water absorption properties. The scaffold incorporated pyrrolidonecarboxylic acid zinc (PC_1Z_2), a compound with anti-inflammatory and moisturizing properties, which was cross-linked within a network of CNTs and a decellularized dermal matrix. The resulting shape-memory sponge scaffold actively interfaces with endogenous electric fields, facilitating electrical signal transmission to skin cells and accelerating tissue repair. Upon exposure to near-infrared (NIR) light, the PC_1Z_2 scaffold enhanced antibacterial efficacy (98 %) through photothermal conversion, promoting tissue metabolism at the wound site. Notably, the scaffold absorbed wound exudates and gradually released Zn^{2+}, effectively reducing chronic inflammation in the mice. In a diabetic rat wound model, the PC_1Z_2 scaffold absorbed exudates, reduced inflammation, and accelerated granulation tissue formation, wound angiogenesis, and re-epithelialization. This innovative PC_1Z_2 sponge dressing shows promise for enhancing the healing of diabetic wounds.

1. Introduction

Diabetic wounds are prevalent and severe complications in patients with diabetes, significantly affecting both morbidity and mortality rates. Routine skin healing involves a series of stages, including hemostasis, inflammation, proliferation, and remodelling [1]. However, this process is often disrupted in patients with diabetes, hyperglycemia, and dyslipidemia. The delayed healing of diabetic wounds can be attributed to various factors. In hyperglycemic and hyperlipidemic wound environments, excess neutrophils are attracted to the wound site, intensifying inflammation by the release of toxic compounds and cytokines. This disrupts the transition of macrophages from a pro-inflammatory to an anti-inflammatory state, thereby prolonging inflammation [2]. Microbial invasion is a crucial factor in the impaired healing of chronic wounds. In diabetic wounds, bacteria proliferate rapidly and form biofilms on the extracellular matrix (ECM), hindering wound healing by disrupting epithelial tight junctions and inhibiting protein synthesis [3]. Chronic hyperglycemia hampers endothelial progenitor cell function and reduces angiogenesis. Consequently, it is imperative to develop safe and efficient multifunctional dressings for diabetic wound treatment [4]

Endogenous electric fields (EFs) induced by wounds have been shown to act as primary signals that direct cell migration and enhance tissue regeneration [5]. Guo et al. revealed that the skin generates an endogenous electric field ranging from 5 μA/cm^2 to 100 μA/cm^2 post-injury [6]. This phenomenon is driven by the movement of cations (predominantly Na^+) from the epidermal cells to the basal layer and anions (Cl^-) to the epidermal layer via ion channels and pumps [7]. Consequently, cations accumulate in the basal layer of the skin, whereas anions gather at the surface, establishing and sustaining a transepidermal potential (TEP) at the site of injury. Electrical stimulation

* Corresponding author.
E-mail address: cedar126@163.com (Q. Zhai).
[1] These authors contributed equally to this work.

https://doi.org/10.1016/j.mtbio.2025.101769
Received 20 January 2025; Received in revised form 24 March 2025; Accepted 11 April 2025
Available online 12 April 2025
2590-0064/© 2025 The Authors. Published by Elsevier Ltd. This is an open access article under the CC BY-NC license (http://creativecommons.org/licenses/by-nc/4.0/).

contributes to pathogen reduction, immune cell and cytokine attraction, mast cell decrease, downregulation of pro-inflammatory cytokine expression, and acceleration of inflammatory phase resolution. Throughout the proliferative phase, diverse cell types, such as endothelial cells, fibroblasts, and epithelial cells, respond to electrical cues, collectively facilitating wound healing [8]. Therefore, the flow of ions across cell membranes is pivotal for EF generation, and any disruption in this process may impede skin repair and regeneration. Scientists have devised a novel electrotactic coupling method to replicate the EF at a wound site and expedite tissue regeneration. This technique involves the use of self-powered dressings (EGDs) with negative-pressure wound therapy [9]. In this treatment system, periodic negative pressure prompts the mechanical deformation of the dressing, producing characteristic pulses with high pressure and low current. These pulses deliver a steady and secure compensatory electric potential to the wound site. This approach mitigates the adverse effects of negative pressure drainage and refines and amplifies the intrinsic electric field of the wound. The electric field produced by EGD triggers robust electrotactic migration responses in epidermal cells and fosters the polarisation of macrophages towards the M2 phenotype. Although external electrical stimulation (ES) can enhance wound healing, current electrotherapy devices are cumbersome, operationally complex, and require consideration of variables such as current parameters, wound conditions, and patient tolerance. Consequently, devising strategies to leverage endogenous electric fields to heal chronic wounds remains challenging.

Carbon nanotubes (CNTs) are cylindrical structures composed of concentrically rolled graphene sheets with a regular arrangement of carbon atoms owing to sp^2 hybridisation. This unique structure confers exceptional electrical conductivity (up to 10^4 S/cm^2) and thermal conductivity (up to 5000 W/m·K) to CNTs, along with their lightweight and highly porous characteristics [16]. Their nanoscale dimensions result in surface roughness and surface area comparable to collagen fibers in the ECM, affecting cell adhesion, proliferation, and differentiation [10]. CNTs exhibit a broad electromagnetic wave absorption spectrum, including near-infrared bands I and II, which are optimal for photothermal conversion in biological tissues and are non-toxic to cells. They can absorb radiation and microwaves and convert them into heat energy, disrupting bacterial membranes and proteins, and leading to bacterial death without inducing resistance [10]. Furthermore, the excellent photothermal properties of CNTs elevate the temperature at the wound sites, promoting vasodilation, enhancing blood circulation, reducing inflammation, increasing capillary permeability, aiding exudate absorption, alleviating tissue edema, and minimizing scar formation [14].

This study leveraged the distinctive photo-detachable characteristics of CNTs to create a novel photothermal-coupled sponge dressing, PC_1Z_2. Zinc pyrrolidone carboxylate, known for its anti-inflammatory and moisturizing properties, was cross-linked with a decellularized dermal matrix interpenetrating network of CNTs to produce a shape memory scaffold. This scaffold was designed to actively modulate immune cell activity. As the PC_1Z_2 scaffold absorbs wound exudates, zinc ions (Zn^{2+}) are gradually released, establishing an endogenous electric field across the wound defect regions. This electric signal is transmitted to the cells participating in wound healing, expediting tissue regeneration. Notably, the PC_1Z_2 sponge scaffold exhibited exceptional photothermal responsiveness and achieved a bacterial eradication rate of 98 %. Additionally, it elevates the temperature at diabetic wound sites, leading to vasodilation, improved blood circulation, and reduced inflammation. Consequently, this versatile sponge scaffold, which integrates bioelectric field coupling, photothermal reactivity, and local immune regulation, holds substantial promise for advancing diabetic wound recovery (Scheme 1).

2. Materials and methods

2.1. Materials and animal welfare

Aminated carbon nanotubes (CNTs) with an amine content of 0.7 mmol/g (purity ≥99 %) were procured from Shenzhen Suiheng Graphene Technology. 1-Ethyl-3-(3-dimethyl aminopropyl) carbodiimide hydrochloride (EDC, 98 %) and N-hydroxysuccinimide (NHS, 98 %), Zinc pyrrolidone carboxylate (Purity ≥97 %) and paraformaldehyde were obtained from Macklin (Shanghai, China). All other chemicals and reagents were obtained from Sigma–Aldrich. Immortalized human umbilical vein endothelial cells (HUVECs) (Product No. LH-H089) were purchased from Baiha Biotech (Shanghai, China). The Cell Bank of Southern Hospital, Southern Medical University provided the L929 cell

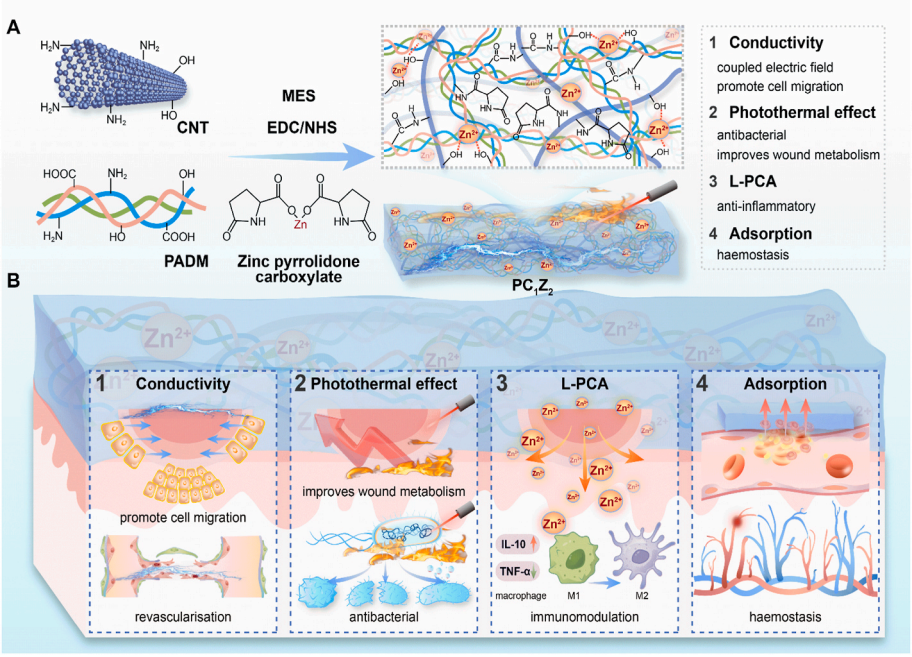

Scheme 1. Schematic flowchart. (A) Preparation of photoelectric-coupled carbon nanotube sponge. (B) Use of a pyrrolidone carboxylate zinc-loaded sponge for the programmed healing of diabetic wounds.

line. Escherichia coli (E. coli) and Staphylococcus aureus (S. aureus) strains were obtained from the Guangzhou Institute of Microbiology.

Male Sprague-Dawley (SD) rats (10 weeks old, weighing 220 ± 10 g) and male white Tibetan miniature pigs (6 months old, weighing approximately 30 kg) were selected as experimental subjects to minimize hormonal interference. The animals were procured from the Animal Research Institute of Southern Medical University (Licence No. SCXK (Yue) 2023-0056) and Guangzhou Huaten Biotechnology (Licence No. SYXK (Yue) 2024-0307). The Institutional Animal Care and Use Committee (IACUC) of the Southern Hospital, Southern Medical University, approved the experimental procedures. The study was conducted according to the guidelines and ethical standards established by the National Science Research Council. The animals were housed under controlled conditions at 21 °C with a 12 h light/dark cycle and provided with water and standard rodent feed after a 7-day acclimation period.

2.2. Preparation of zinc pyrrolidonecarboxylate-loaded carbon nanotube/porcine decellularized dermal matrix sponge scaffold

Porcine decellularised dermal matrix (PADM) was prepared according to previously established protocols [11,12]. Initially, the PADM powder was dissolved in 1 % acetic acid aqueous solution to achieve a concentration of 1 % (w/v) aqueous acetic acid solution. Various mass ratios (0.5, 1, and 1.5 % (w/v)) of CNTs were subsequently added to the DDM solution, which was then freeze-dried to produce a sponge. The resulting sponge was immersed in an EDC (5 mM)/NHS (10 mM) crosslinking solution for 36 h. Following extensive washing with deionised water, the sponge underwent another freeze-drying cycle to yield the CNT-PADM sponge (PC). Different mass ratios (0.5, 1, 2, and 4 %) of zinc pyrrolidone carboxylate were incorporated into the optimized CNT-PADM solution, and the sponge was subjected to the same EDC/NHS crosslinking process for 36 h. Subsequent washing with deionised water and a final freeze-drying step resulted in a zinc-loaded sponge (PCZ) structure.

2.3. Characterization of physicochemical properties of the sponge

The morphology of the scaffolds was assessed using a digital camera (Samsung S23 Ultra) and scanning electron microscope (Regulus 8100, Hitachi, Japan). Elemental composition analysis of carbon (C), nitrogen (N), oxygen (O), and zinc (Zn) on the surface of the samples was conducted using energy-dispersive X-ray fluorescence (EDXRF). Chemical functional group alterations in the materials were examined employing attenuated total reflection Fourier-transform infrared spectroscopy (ATR-FTIR, Nicolet iS50 FT-IR, Thermo Fisher, USA) and Raman spectroscopy (Renishaw RM2000, Renishaw, UK). The porosity, water absorption, and density of the sponges were quantified using a porosity tester (JHY-120C).

Compression tests were conducted on dry and wet sponges using a universal testing machine(DR-603A) by applying 10 cycles of 60 % compression to each sample. Stress-strain curves were generated, and the compression modulus was calculated. Additionally, cylindrical sponge samples were soaked in deionised water under uniform pressure to observe and document sponge morphology before, during, and after compression. The hydrophilic/hydrophobic characteristics of the sponges were evaluated using a contact angle/surface tension instrument (Theta Flex, Biolin, Finland).

The water retention capacity of the sponges was assessed by immersing cylindrical samples (1.2 cm in diameter and 1.4 cm in height) in deionised water and recording their initial weight as W0. Subsequently, the samples were incubated at 37 °C, intermittently removed, and weighed at specified time intervals (Wt). The water retention rate was determined using the following equation: water retention rate = Wt/W0.

Electrical conductivity testing was performed on the four types of scaffolds by soaking them in pure deionised water for three days, with a minimum of five water changes to eliminate residual impurities and ions from the manufacturing process. Subsequently, each sample was immersed in deionised water in a 50 mL centrifuge tube at 37 °C for 2 h to absorb water. The electrical conductivity was assessed using a four-point probe resistivity meter (KDY-1), and the conductivity of the sponge was evaluated by integrating it into a circuit with a conductive LED for testing.

The dry weight of the sponge was initially measured, followed by its weight after complete water absorption. Subsequently, a weight of 100 g was applied to the sponge for 5 min, and the water absorption was re-evaluated. The procedure was repeated five times. The phase compositions of the samples were assessed via X-ray diffraction (XRD, SmartLab SE Rigaku, Japan), and their thermal stabilities were determined using a thermogravimetric/differential scanning calorimeter (TGA/DSC 3+, Mettler Toledo, Switzerland).

2.4. Zn^{2+} release experiment

The PC_1Z_2 sponge (100 mg) was immersed in 10 mL of PBS at 37 °C. The container was sealed and placed in a constant temperature shaker (100 rpm) at 37 °C to simulate the in vitro release. At predetermined time points, 100 μL of the solution was collected for testing, and an equal volume of fresh PBS was added. The collected samples were digested with nitric acid, and the Zn^{2+} concentration was measured using inductively coupled plasma atomic emission spectroscopy (Agilent 7700; Agilent, USA).

2.5. Antibacterial performance evaluation

E. coli (ATCC 25922) and S. aureus (ATCC 6538) were selected as test strains to assess the antibacterial activity of the sponge scaffolds. Sterilized circular sponge (8 mm diameter and 1 mm height) were placed in a 24-well plate. Then, 2 mL of bacterial suspension (10^7 CFU/mL) was pipetted onto the sponge, ensuring complete immersion to facilitate sufficient interaction between the sample and bacteria. Subsequently, the sponge was irradiated with NIR (808 nm, 1 W/cm^2) for 15 min, followed by incubation in a shaker at 37 °C for 36 h. After incubation, the bacterial suspension was serially diluted (10^5 fold) using LB broth. A 100 μL aliquot of the diluted suspension was evenly spread on blood agar plates (Kailin, P0901) and cultured at 37 °C for 24 h. The plates were photographed, and the number of colonies was counted to evaluate the antibacterial efficacy of each sample. Each test was performed in triplicates. The bacterial suspension co-cultured with the sponge was fixed overnight using 2.5 % glutaraldehyde. The samples were then dehydrated using a graded ethanol series and dried at room temperature in a vacuum desiccator. Finally, the microscopic morphology of the bacteria was examined using scanning electron microscopy.

Furthermore, the sponge and bacterial suspension system was irradiated with NIR (808 nm, 1 W/cm^2) for 15 min. The sponge and bacterial suspensions were transferred to a centrifuge tube and subjected to high-speed centrifugation at 12,000 rpm for 5 min to pellet the bacterial cells. After centrifugation, the bacterial pellet was washed with phosphate-buffered saline (PBS) and centrifuged again. The pellet was then resuspended for subsequent use. A live/dead bacterial staining kit (DMAO/PI) (Beyotime, C2030S) was used. DMAO stained both live and dead bacteria green, whereas PI specifically stained dead bacteria red. After staining, the bacterial suspension was washed thrice with PBS and centrifuged to remove the supernatant. The pellet was gently resuspended, and a droplet of the suspension was placed on a glass slide, covered with a cover slip, and stored in the dark. Finally, the samples were observed, recorded, and photographed using an inverted fluorescence microscope (Nikon ECLIPSE Ti). All procedures were performed in triplicate to minimize experimental error.

2.6. Live/dead cell staining and cellular morphology staining

Cell cytotoxicity was evaluated on days 1, 2, and 3 of culture using the CCK-8 assay (Apexbio, K1018, USA) according to the manufacturer's protocol. To further explore the biocompatibility of the scaffold extract, live/dead cell staining (Invitrogen, L3224, USA) was performed. Because dye absorption by the scaffolds hinders cell morphology observation, the cells were co-cultured with scaffold extracts in selected trials to facilitate observation. Specifically, L929 or HUVEC cells were seeded at 1.0×10^4 cells/well on tissue culture plates (TCP), and an equivalent amount of scaffold was incubated in serum-free medium for three days. The resulting supernatant was harvested, and 10 % fetal bovine serum (FBS) was added to the culture medium. Standard culture medium was used as the control. Subsequently, on days 1, 2, and 3, the cells were stained with a live/dead stain (calcein-AM/PI, E-CK-A354) for 30 min and visualized under an inverted fluorescence microscope (Nikon ECLIPSE Ti). Calcein-AM stained live cells green, and PI stained dead cells red. All experiments were performed in triplicate to ensure the precision of the results.

Following a 48 h co-cultivation of L929 cells with scaffold extracts, the culture medium was renewed, and the cells were fixed with 4 % paraformaldehyde for 20 min at room temperature. The staining protocol involved permeabilization with 0.1 % Triton X-100 for 5 min at room temperature, blocking with 1 % BSA in PBS for 30 min, and staining with 200 μL of Cyto-Red peptide dye for 20 min. Subsequently, the cells were counterstained with DAPI for 5 min to visualize the nuclei. Between each step, the samples were washed thrice with PBS. Cellular morphology was assessed using a ZEISS/LSM 980 laser-scanning confocal microscope.

2.7. In vitro anti-inflammatory and angiogenesis evaluation

RAW 264.7 macrophages and HUVECs were used as experimental models to evaluate the anti-inflammatory and proangiogenic effects of sponge dressings. Initially, both cell types (5×10^4 cells per well) were seeded in standard and confocal cell-culture plates and incubated for 12 h. Subsequently, the cells were rinsed with PBS. A solution containing 500 ng/mL lipopolysaccharide (LPS) and blank medium was administered to the positive control group. In contrast, the experimental group was treated with 500 ng/mL LPS and 2 mg/mL of the sponge extract in the culture medium. The negative control group was exposed to a blank medium. Following a 36 h incubation period, the cells were washed with PBS, fixed with 4 % paraformaldehyde, and blocked with 1 % BSA for 30 min. Subsequently, the cells were incubated overnight at 4 °C with primary antibodies and then with secondary antibodies at room temperature for 1.5 h. Tumor necrosis factor-α (TNF-α) served as the primary antibody for RAW 264.7 cells, while vascular endothelial growth factor (VEGF) was used for HUVECs. The secondary antibody was FITC-conjugated affinity-purified goat anti-rabbit IgG (H + L). Fluorescently labelled cells were visualized using a laser scanning confocal microscope (ZEISS/LSM LSM 980). All experiments were performed in triplicate.

2.8. Scratch assay

L929 cells and HUVECs cultured to the logarithmic phase were digested and prepared into cell suspensions at 2×10^5 cells/mL. Cell suspensions were seeded into 12-well plates. Once the cells had adhered, the culture medium was replaced with serum-free high-glucose DMEM for 24 h starvation treatment. Next, two parallel lines were drawn on the cell monolayer using a 200 μL pipette tip. The cells were washed 2–3 times with PBS to remove any debris. Subsequently, a sponge scaffold was placed into the transwell chamber and transferred to an incubator for further incubation. Cell growth was observed at different time points by photographing under a microscope.

2.9. In vitro whole blood clotting time

The in vitro clotting activity of the material was assessed by determining the whole blood clotting time. Fifty milligrams of sponge material was placed in a sterile centrifuge tube, and 2 mL of anticoagulated pig whole blood and 100 μL of 0.2 mol/L $CaCl_2$ solution were added. The tubes were incubated at 37 °C with gentle tilting every 5 s to monitor the clot formation. The time from the addition of blood to complete clot formation was recorded as the in vitro clotting time. Each sample was tested in triplicates.

2.10. Hemolysis activity test

Hemolysis was evaluated by quantifying the absorbance of blood cells post-incubation with the specimens. First, 1 mL of porcine whole blood was diluted with 5 mL of normal saline (NS). Subsequently, 0.5 cm × 0.5 cm) were immersed in 1 mL of NS at 37 °C for 1 h to generate a suspension. Next, 100 μL of pre-diluted porcine blood was added to the sample suspension to form the experimental group. NS and deionised water were used as negative and positive controls, respectively. All samples were incubated at 37 °C for 1 h and subsequently centrifuged at 1500 rpm for 10 min. The resultant supernatant was harvested, and the absorbance at 540 nm was determined using a microplate reader (OD value). The hemolysis percentage was calculated using the following equation: Hemolysis rate (%) = (OD material well-OD negative well)/(OD positive well-OD negative well) × 100. The experiment was repeated thrice.

2.11. In vitro coagulation assay

The in vitro coagulation efficacy of the sponge was assessed using the blood coagulation index (BCI) of healthy pig whole blood anticoagulated with sodium citrate. Samples of uniform size (1.0 cm × 1.0 cm) were incubated in culture dishes at 37 °C for 5 min. Subsequently, 100 μL of activated pig blood (activated with 0.2 M $CaCl_2$) was added to each sample. A blank culture dish (TCP) was treated with 100 μL of activated blood as a negative control. Following a 5 min incubation at 37 °C, 20 mL of deionised water was gently introduced to wash away non-coagulated blood, facilitating haemoglobin release. After an additional 10 min incubation at 37 °C, the absorbance of the haemoglobin solution at 540 nm (Abs1) was quantified using a microplate reader. A blank control was established by mixing 100 μL of whole blood with 20 mL of deionised water (Abs0). Each experimental group was evaluated in triplicate. BCI was determined using the following formula: BCI (%) = (Abs1/Abs0) × 100 %.

2.12. Blood cell adhesion experiment

Red blood cell (RBC) and platelet adhesion to sponge materials were examined using scanning electron microscopy. Fresh, anticoagulated porcine whole blood samples were collected. A 100 μL portion of whole blood was applied to a 1 cm × 1 cm sponge and incubated at 37 °C for 30 min. Subsequently, the samples were washed thrice with PBS to eliminate non-adherent blood cells. The samples were then immersed in 1 mL 2.5 % glutaraldehyde at room temperature for 2 h, followed by rinsing with PBS. Sequential dehydration was performed using increasing ethanol concentrations (50, 60, 70, 80, 90, and 100 %) for 10 min each. Following dehydration, the samples were air-dried and examined using SEM to assess the aggregation and adhesion of red blood cells (RBCs) and platelets.

2.13. Liver hemostasis test in sprague dawley rats

Following intraperitoneal injection of 2 % sodium pentobarbital for anesthesia, the rats underwent abdominal hair removal. An incision measuring 1–2 cm was performed 1 cm below the xiphoid process to

expose the liver. Subsequently, a 1 cm long and 0.5 cm deep incision was made on the liver surface to facilitate 2 s of unimpeded blood flow, after which a pre-weighed sponge sample was applied for hemostasis. The coagulation time was documented, and the weight of the sponge before and after blood absorption was measured. The experiment was conducted thrice for each rat.

2.14. Tail amputation hemostasis test in sprague-dawley rats

One-third of the tail was amputated after intraperitoneal anesthesia with 2 % sodium pentobarbital. Upon the initial appearance of blood, various pre-weighed sponge dressings were promptly placed at the bleeding site to stop the bleeding. The clotting time was documented, and the weight of the sponge dressings after blood absorption was assessed. This procedure was repeated thrice.

2.15. In vivo wound healing experiment

SD rats were randomly allocated to four groups: Control, Collagen Sponge (CS), PC_1, and PC_1Z_2. Diabetes was induced by intraperitoneal administration of 1 % streptozotocin (STZ) solution at 65 mg/kg every other day. Successful establishment of the diabetic model was confirmed after one week based on the presence of polydipsia, polyphagia, polyuria, and random blood glucose levels exceeding 16.7 mmol/L. After 2 % sodium pentobarbital anesthesia, the rats were placed in a prone position on a mouse board. Following shaving and disinfection of the backs, two full-thickness skin defects (12 mm in diameter) were generated. The wounds were dressed with sponges and secured with gauze, except in the control group. The dressings were changed every 48 h, and dislodged sponges were immediately replaced. The in vivo photothermal characteristics of the materials were evaluated by exposing the skin implants to 808 nm NIR light for 10 min, twice daily. Wound healing progress was monitored and documented on postoperative days 0, 3, 7, 14, and 21. Tissue samples (0.5 cm around the wound margin) were collected at each time point, fixed in 4 % paraformaldehyde, embedded in paraffin, and sectioned. Epithelialization, collagen deposition, angiogenesis, and scar formation were evaluated using hematoxylin and eosin (H&E) staining, Masson's trichrome staining, and immunohistochemical staining (IL-10, TNF-α, CK14, CD31, and Ki67). The extent of collagen deposition in the wound area was quantified using ImageJ, and immunohistochemical markers were analyzed quantitatively using Image J software.

2.16. Statistical analysis

SPSS 20.0 software was used for this statistical analysis. All quantitative data sets are presented as mean ± standard deviation (SD). Differences between groups were analyzed by one-way analysis of variance (ANOVA), followed by Tukey's post hoc test. Statistical significance is considered * $p < 0.05$, ** $p < 0.01$, *** $p < 0.001$. All in vitro and in vivo data were analyzed using GraphPad Prism software (version 8.0).

3. Results and discussion

3.1. Preparation and characterization of carbon nanotube-decellularized dermal matrix sponges

Multiwalled carbon nanotubes have tubular structures comprising hexagonal carbon rings and end caps composed of pentagonal carbon rings. This distinctive and stable configuration renders it nearly insoluble in various solvents, including water and common organic solvents. CNTs tend to aggregate, bend, and intertwine in solution owing to strong van der Waals forces, leading to the formation of bundles [13]. This aggregation hinders molecular-level studies and results in poor biocompatibility, significantly constraining their potential applications in the biomedical field. Compared to pristine CNTs, amine-modified CNTs demonstrate enhanced solubility, reactivity, bioactivity, reduced cytotoxicity, improved cellular penetration, and superior biocompatibility, establishing a robust basis for their use in pharmaceutical applications [14]. Ongoing investigations into aminated CNTs in pharmaceutical contexts have predominantly focused on their function as carriers of drugs or genes in bioengineering, DNA and vaccine delivery, and tissue regeneration, showing promising advancements [15].

The aminated CNTs were crosslinked with PADM via amide and hydrogen bonds, forming a sponge network structure via freeze-drying (Fig. 1A). The multiwalled CNTs exhibited a concentric circular structure owing to the interactions between the coaxial tubes via van der Waals forces (Fig. 1B). The TEM images revealed the tubular structure of the multiwalled CNTs, consisting of multiple coaxial carbon layers with diameters ranging from 10 to 30 nm and lengths of 1–2 μm (Fig. 1C). The surface functional groups on CNTs influence the vibrational frequencies of the carbon atoms, which can be assessed using Raman spectroscopy [16]. The D-band peak at 1350 cm^{-1} indicates the presence of sp3 hybridized carbon atoms or defects in the sp2 hybridized carbon network, with the intensity reflecting the defect level in the CNTs. The G band peak at 1590 cm^{-1} corresponds to sp2 hybridized carbon atoms, while the weak peak at 3450 cm^{-1} signifies the stretching vibration of N-H (Fig. 1D).

Fourier-transform infrared spectroscopy was used to analyze the structural modifications of the sponges. The pristine CNTs exhibited two minor absorption peaks at 1023 cm^{-1} and 1538 cm^{-1}, corresponding to the C-C backbone vibration of the CNTs. The peak at 1430 cm^{-1} corresponds to the distinctive absorption peak of the amide bond (Amide II) arising from N–H bending and C-N stretching vibrations. A noticeable C-N stretching vibration peak was evident at 1157 cm^{-1}, along with a bending vibration peak of the secondary amine N-H at 700 cm^{-1}. These characteristic peaks confirm the grafting of amine compounds onto the CNTs. The PADM sponge displayed absorption peaks at 1537 cm^{-1} and 1643 cm^{-1}, which aligned with the characteristic absorption peaks of collagen amino groups. In the $PC_{0.5}$, PC_1, and $PC_{1.5}$ groups, the absorption peaks at 1640 cm^{-1} (Amide I, C=O stretching), 1508 cm^{-1} (amide II, N-H bending), and 1231 cm^{-1} (amide III, C-N stretching) (Fig. 1E) confirmed the establishment of amide bonds between the CNTs and PADM [17].

The PADM sponge initially appeared white but became dark black as the CNT content increased. No significant swelling was observed during the water absorption process (Fig. 1G). Microscopic examination of all sponges revealed a porous network structure (Fig. 1H), indicating that the addition of CNTs did not compromise the structural integrity of the scaffold. The porous nature of the sponge facilitates effective blood contact, thereby promoting the coagulation cascade. Contact angle measurements were performed to evaluate the changes in hydrophilicity and hydrophobicity. A higher contact angle (θ) indicates lower wettability and stronger hydrophobicity, whereas a lower θ indicates higher hydrophilicity. As shown in Fig. 1I, all the sponges demonstrated a degree of hydrophilicity that increased with the incorporation of CNTs. In particular, PC_1 sponge exhibited rapid water absorption within 2 s, likely due to the presence of abundant active groups such as -OH and C=O on the surface after CNT crosslinking with PADM, which enhanced the hydrophilicity of the sponge. Dynamic quantitative analysis (Fig. 1F) further supports this observation [18].

Normal skin possesses distinctive mechanical strength and elasticity, which are crucial for skin substitutes. A compression test was conducted on the sponges to assess their mechanical compressive properties over 10 cycles by analysing the stress-strain curves and Young's modulus at 60 % compression (Fig. 1J–M). The PADM scaffold exhibited a maximum stress of 4.8 kPa during the initial compression cycle, whereas the $PC_{0.5}$, PC_1, and $PC_{1.5}$ scaffolds showed maximum stresses of 8.3, 9.2, and 9.4 kPa, respectively. The compression curves for the 5th and 10th cycles were nearly identical, with Young's moduli for the $PC_{0.5}$, PC_1, and $PC_{1.5}$ groups measured as 0.30 ± 0.03 MPa, 0.43 ± 0.04 MPa, and 0.46 ± 0.03 MPa, respectively. These findings suggest that the PC_1 and $PC_{1.5}$

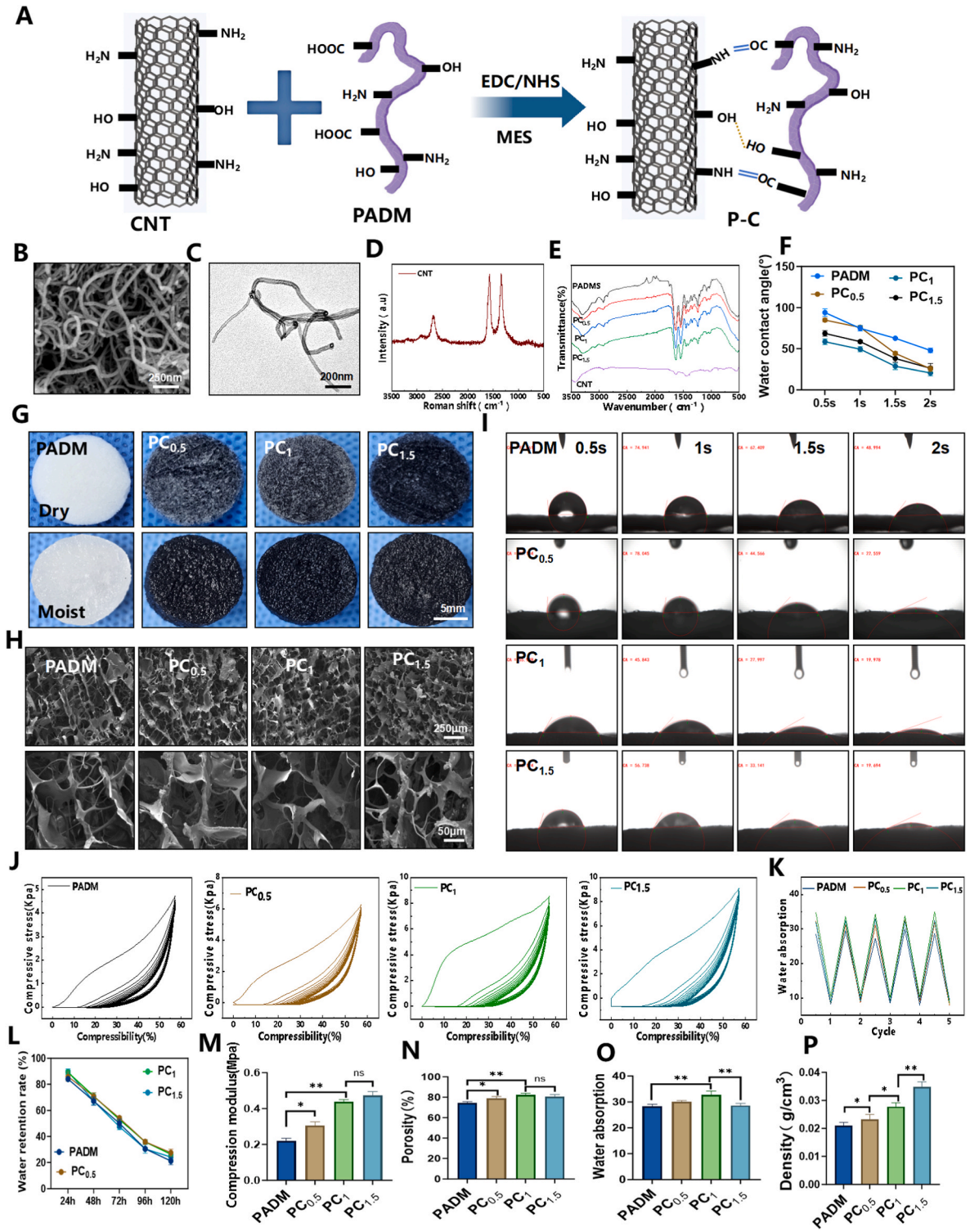

Fig. 1. Preparation and characterization of carbon nanotube-decellularized dermal matrix sponge. (A) Schematic representation of sponge preparation. (B) Microstructural analysis of carbon nanotubes. (C) Transmission electron microscopy. (D) Raman spectroscopic. (E) Fourier-transform infrared spectroscopy. (F) Quantification of the water contact angle. (G) Macroscopic images. (H) Microscopic images. (I) Dynamic water contact angle image. (J) Compressive stress-strain curves. (K) Water absorption curves of various scaffolds over cycles. (L) Water retention rate. (M) Compressive modulus. (N) Porosity. (O) Water absorption rates. (P) Density. (*$p < 0.05$, **$p < 0.01$, ***$p < 0.001$).

scaffolds offer enhanced mechanical stability compared with PADM scaffolds. Notably, these scaffolds exhibited reversible water absorption properties. As depicted in Fig. 1K, applying 80 % strain to compress the scaffolds effectively removed most of the absorbed water, which was then reabsorbed upon release of the compression force, restoring the scaffold to its original shape [19]. After five compression cycles, the maximum water absorption rates of the scaffolds remained consistent, with no significant hysteresis, indicating their reversible water absorption capability. Furthermore, CNT-based scaffolds demonstrated exceptional water retention, with the PC_1 scaffold retaining the highest

water content at 23.5 ± 1.2 % after 120 h, as illustrated in Fig. 1L.

The wettability and water absorption characteristics of scaffold materials are crucial for determining cell viability. The enhanced water absorption capacity of the scaffolds facilitates tissue regeneration by efficiently absorbing excess biological fluids at the wound site, thereby reducing the risk of infection [20]. To assess the moisture absorption behavior, we analyzed the water absorption properties of the scaffolds before and after their modification. As shown in Fig. 1O, all scaffolds reached their maximum water absorption capacity and swelled within 30 s of contact with water, with the PC_1 group exhibiting the highest water absorption. This is likely attributed to the high specific surface area and excellent hydrophilicity of carbon nanotubes (CNTs), which enhance the water absorption capability of the sponge. Additionally, incorporating CNTs increased the internal pore structure of the sponge, thereby improving its porosity. However, when the mass-to-volume ratio of CNTs exceeded 1 %, the internal structure of the sponge became increasingly compact. Although the water absorption capacity continued to increase, it did not surpass the rate of mass increase, leading to a decline in the sponge water absorption rate. As illustrated in Fig. 1N, the porosity of the sponge improved to some extent with increasing CNT content. However, when the CNT content reached 1 % (PC_1), the porosity of the sponge peaked, and further increases in the CNT content did not result in a significant increase in porosity. This may be because the CNTs were uniformly dispersed within the decellularized dermal matrix, forming a stable porous network structure. CNTs possess high strength and flexibility, enabling them to create self-supporting pore structures within the sponge. Even with an increased CNT content, the pores did not easily collapse or become blocked. When the CNT content reached 1 %, its impact on the porosity of the sponge reached a saturation point. Moreover, sponge density increased with increasing carbon nanotube (CNT) content (Fig. 1P). In summary, incorporating CNTs significantly enhanced the physicochemical properties of pure PADM sponges, and optimal properties were achieved with a CNT content of 1 % (PC_1). Therefore, PC_1 was selected for subsequent experiments in this study.

3.2. Preparation and characterisation of zinc-pyrrolidone carboxylate-loaded carbon nanotube-decellularised dermal matrix sponges

Zinc pyrrolidone carboxylate, the zinc salt of L-pyrrolidone carboxylic acid (L-PCA), is a water-soluble compound found in the stratum corneum of the skin. It exhibits moisturizing properties and possesses antimicrobial, anti-inflammatory, and regulatory properties. These characteristics enhance the skin barrier function, reduce water loss, and sustain skin integrity by ensuring prolonged hydration [21]. This study introduced zinc-pyrrolidone carboxylate, known for its anti-inflammatory and moisturizing effects, into the PC_1 matrix to create a molecularly interpenetrating network structure. The sponge samples exhibited a uniform black appearance with interconnected pore structures (Fig. 2C), indicative of a three-dimensional network, as illustrated in Fig. 2B. This architecture offers a large surface area for cell adhesion and facilitates tissue infiltration after in vivo implantation, thereby expediting degradation over time. As the zinc-pyrrolidone carboxylate content increased, the hydrophilicity of the sponges improved (Fig. 2D). In particular, the PC_1Z_2 sponge demonstrated the lowest water contact angle (17 ± 3.42°), with statistically significant differences observed among the groups (Fig. 2H) ($p < 0.01$). Notably, the PC_1Z_2 sponge exhibited distinctive water-induced shape-recovery properties. Upon water infiltration, the compressed PC_1Z_2 sponge promptly absorbed the liquid, expanded to regain its original volume, and nearly reverted to a cylindrical shape after external compression (Fig. 2E). Elemental mapping analysis (Fig. 2G) indicated that the PC_1Z_2 sponge comprised carbon, nitrogen, oxygen, and zinc, which were evenly distributed throughout the pores [12].

The wettability and water absorption characteristics of the scaffold materials significantly affected cell viability. Enhanced water absorption in sponges facilitates tissue regeneration by efficiently draining excess biological fluids from wounds, thereby reducing the risk of infection [22]. Fig. 2F shows the gradual increase in the water absorption rate of the sponges with increasing zinc-pyrrolidone carboxylate content, with the PC_1Z_2 sponge displaying the highest water absorption rate (39 ± 1.4 %). Moreover, compared to PC_1 group, the inclusion of zinc pyrrolidone carboxylate enhanced the porosity of the sponges, reaching peak porosity (91.4 ± 1.3 %) at 2 % zinc pyrrolidone carboxylate content (PC_1Z_2) (Fig. 2I). This is because, in the PC_1Z_2 gel, tiny ice crystals formed from water were able to grow and aggregate, and some tiny crystals were excluded during the growth process, resulting in ice crystals of varying sizes that formed large pores with smaller pores after freeze-drying, exhibiting a high porosity [23]. The interaction between zinc-pyrrolidone carboxylate and the PC_1 matrix results in a synergistic effect through the association or dissociation of different water-soluble gel molecules, forming a coupled network gel. This molecular swelling caused the gel blocks to increase in volume compared to the original solution, creating a sponge-like volume after gel treatment [21]. To ensure stable conductivity for the transmission of long-term bioelectrical signals, which are critical for cell/tissue function, we evaluated the conductivity of these samples under wet conditions. Increasing the zinc-pyrrolidone carboxylate content led to a stepwise increase in sponge conductivity (Fig. 2J), indicating that the PCZ sponges responded to endogenous bioelectric fields and transmitted bioelectrical signals while maintaining long-term stability upon absorbing wound exudates [24]. The integration of the PC_1Z_2 sponge into the circuit resulted in brighter LED light emissions under wet conditions (Fig. 2K). Fig. 2N illustrates the water-retention capacity of the composite sponges. After a three-day desiccation period, the wet weights of the swollen composite sponges were measured. An increase in the zinc-pyrrolidone carboxylate content corresponded to a gradual enhancement in the water retention capability of the composite sponges, resulting in water retention rates of 6, 7, 10, and 8 % for $PC_1Z_{0.5}$, PC_1Z_1, PC_1Z_2, and PC_1Z_4, respectively, until it peaked at PC_1Z_2, followed by a subsequent decline. The water absorption and retention rates of sponges are governed by sponge porosity, the intrinsic characteristics of carbon nanotubes, and the decellularized dermal matrix. Higher porosity facilitates increased water molecule ingress, augmenting water absorption and retention capacities. Conversely, the interactions between zinc pyrrolidone carboxylate and PC_1 system molecules, along with the quantity of available basic and hydroxyl groups, are contingent on the zinc pyrrolidone carboxylate concentration, which consequently modifies the internal structure and properties of the sponge [21]. At 2 % zinc pyrrolidone carboxylate content, the minimal shielding effect between molecules facilitated the enhanced utilization of basic and hydroxyl groups, resulting in a sponge with an increased abundance of hydrophilic groups capable of forming hydrogen bonds with water molecules, thereby improving the water retention performance [21]. Diabetic wounds are often characterized by a hyperglycemic and chronic inflammatory microenvironment, which results in a slow healing process. Therefore, slow and effective ion release is crucial for the entire healing process. As shown in Fig. 2L, Zn^{2+} were released at a rate of 64.5 ± 1.2 % over 14 days, with the release peaking on the fifth day at 0.56 ± 0.03 mg/L, followed by a gradual and sustained release (Fig. S1). Zinc pyrrolidone carboxylate is a zinc complex that gradually releases Zn^{2+} in an aqueous solution. Zn^{2+} undergo hydrolysis in water, generating hydrogen ions (H^+), as described by the following reaction: $Zn^{2+} + 2H_2O \rightleftharpoons Zn(OH)_2 + 2H^+$. This reaction increases the concentration of hydrogen ions in the solution, lowering the pH (increasing the acidity of the solution). As Zn^{2+} are released, hydrolysis begins, and the concentration of hydrogen ions gradually increases, causing the pH to decrease slowly. With continued Zn^{2+} release, the hydrolysis reaction accelerates, further reducing the pH and increasing the acidity of the solution. When the Zn^{2+} release reaches equilibrium or the Zn^{2+} concentration approaches saturation, the pH change stabilizes but may remain relatively low (Fig. S2). The thermal stability of the composite sponges was

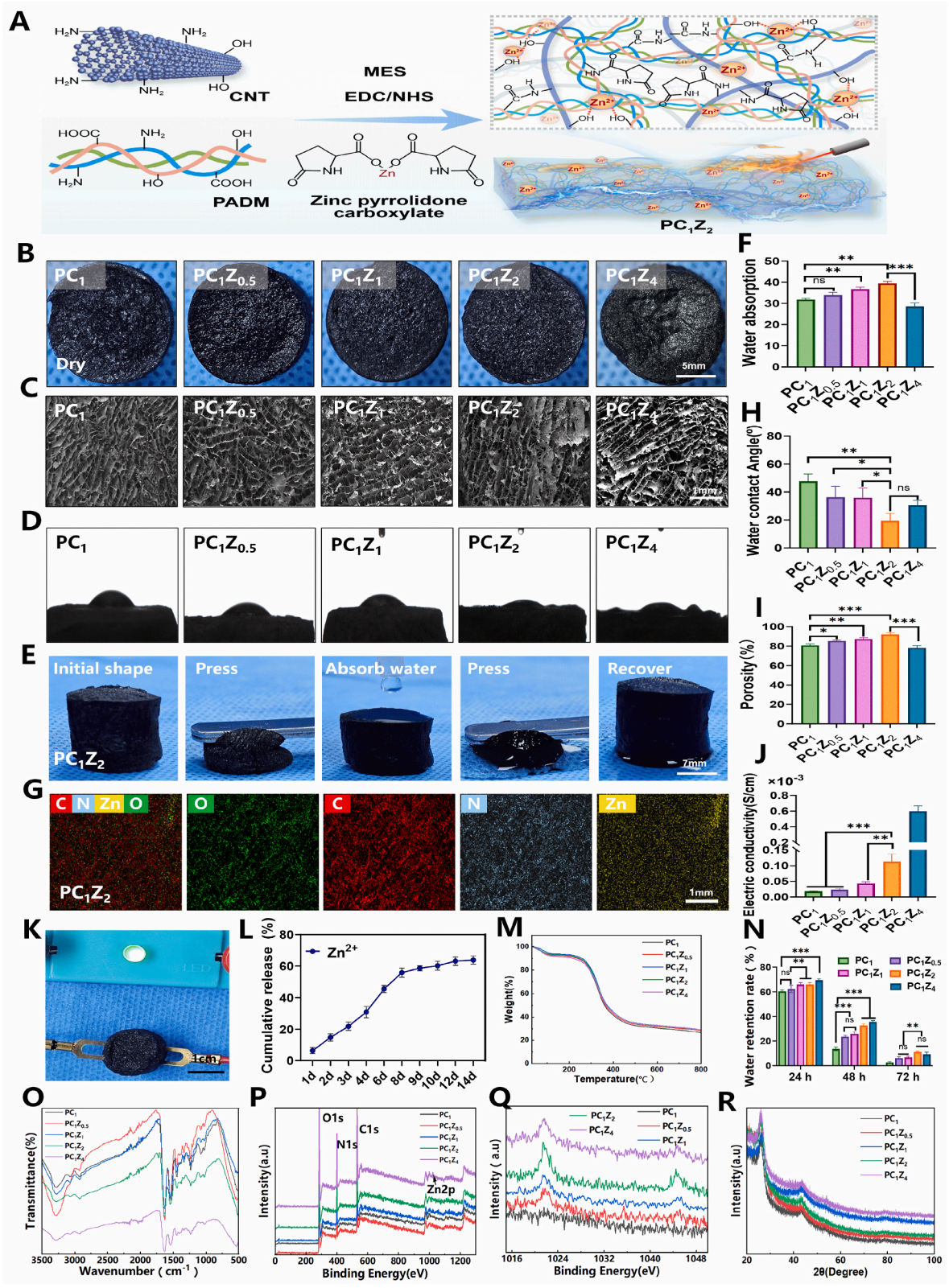

Fig. 2. Preparation and characterization of carbon nanotube-decellularized dermal matrix sponges loaded with zinc-pyrrolidone carboxylate. (B)PC_1Z_2 sponge preparation process. (B) Morphologic image of sponge. (C) Microscopic image of sponge. (D) Images of the water contact angles. (E) Shape memory properties of the PC_1Z_2 sponge. (F) Water absorption. (G) Elemental mapping spectra of PC_1Z_2 sponge. (H) Quantification of water contact angles. (I) Porosity. (J) Wet conductivity assessment of the sponge. (K) Integration of the PC_1Z_2 sponge into a circuit for LED illumination in a humid environment. (L) Release rate of Zn^{2+} from the PC_1Z_2 sponge. (M) TGA. (N) Water retention rate. (O) FTIR. (P) XPS. (Q) Zn 2p XPS spectrum of ZnO. (R) XRD. (*$p < 0.05$, **$p < 0.01$, ***$p < 0.001$).

evaluated using thermogravimetric analysis (TGA), which revealed a triphasic thermal degradation pattern for the sponges. Initially, between 50 °C and 230 °C, a weight reduction of approximately 10 % was observed, which was attributed to the desorption of bound water within the sponge matrix. Subsequently, a substantial weight loss of approximately 50 % occurred between 270 °C and 350 °C, signifying the disintegration of the sponge's structural framework and the removal of hydroxyl groups from neighboring molecular chains as water vapor. The final degradation phase involves the oxidation and disintegration of the carbonized residue. The curve shows that the incorporation of zinc pyrrolidone carboxylate (Zn-PCA) had no significant impact on the thermal stability of the sponge. This is likely due to the inherent high thermal stability of Zn-PCA, which provides a protective effect on the PCZ sponge system. Consequently, the thermal decomposition behavior of the decellularized dermal matrix dominated. Because there are no significant chemical interactions between Zn-PCA and the matrix or

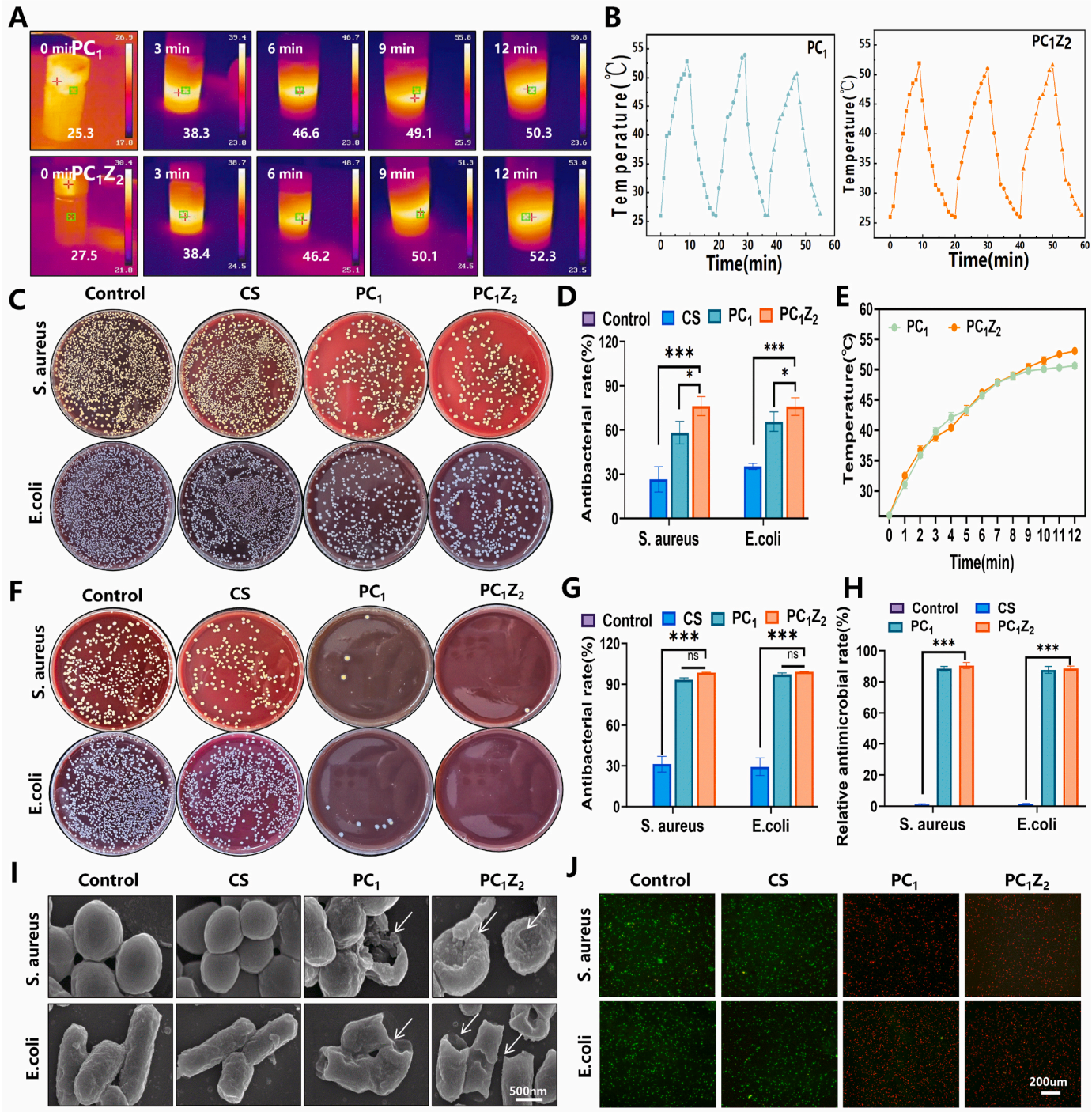

Fig. 3. Evaluation of the photothermal antibacterial performance of the sponges. (A) Images of sponges under NIR laser irradiation. (B) Photothermal cycling curves of the sponges. (C) Colony plate image of a sponge without NIR irradiation is needed. (D) Antibacterial inhibition rate of sponges without NIR irradiation. (E) Temperature change curve of the sponge under NIR laser irradiation. (F) Colony plate image of a sponge after NIR irradiation. (G) Antibacterial inhibition rate of the sponge after NIR irradiation. (H) Relative antibacterial inhibition rates of live and dead bacterial. (I) Microscopic morphology of the bacteria. (J) Images of bacteria stained with live/dead stain. ($*p < 0.05$, $**p < 0.01$, $***p < 0.001$).

carbon nanotubes, its influence on the thermal stability of the sponge system is not pronounced [25].

FTIR analysis of the scaffold revealed the internal interactions within the material. As shown in Fig. 2O, the characteristic absorption peaks of PADM appear at 3277 cm^{-1}, 1628 cm^{-1}, and 1526 cm^{-1}, corresponding to hydrogen bonding between -OH and -NH_2 groups, the amide I band of random coils and helical conformations, and the amide II band of N-H bending vibrations, respectively. The absorption peaks at 1543 cm^{-1} and 1645 cm^{-1} represent the -N-H stretching of amide bonds, indicating that chemical reactions between PADM and aminated carbon nanotubes during cross-linking generate amide bonds [26]. As the proportion of zinc pyrrolidone carboxylate in PC_1 increased, the amide I and amide II bands exhibited a noticeable shift toward higher wavenumbers. Specifically, the characteristic peaks of gelatin at approximately 1630 cm^{-1} (amide I) and 1541 cm^{-1} (amide II) shifted to approximately 1651 cm^{-1} and 1580 cm^{-1}, respectively. This shift suggests the formation of strong intermolecular interactions, particularly electrostatic attraction between the positively charged amide groups in the PC_1 system and the negatively charged groups in zinc pyrrolidone carboxylate. These interactions are hypothesized to reduce the bond length of the -NH functional groups, thereby increasing the wavenumber of the associated spectral bands. Furthermore, after the addition of zinc pyrrolidone carboxylate, significant peak shifts were observed within PC_1 owing to hydrogen bonding interactions [27]. The bending vibration of the amide II N-H band redshifts to 1531 cm^{-1}, indicating interactions between PC_1 molecules and zinc pyrrolidone carboxylate [28]. Specifically, the protonated amino groups in the PC_1 system electrostatically interacted with the carboxyl groups of zinc pyrrolidone carboxylate, promoting the formation of ionic crosslinking. These electrostatic interactions contribute to the formation of a more compact network. Furthermore, as shown in Fig. 2P, the characteristic peaks of Zn elements were observed in the XPS spectra of the sponge (Fig. 2Q). With an increase in the zinc pyrrolidone carboxylate content, the intensity of the Zn characteristic peaks also increased, further confirming the successful incorporation of zinc pyrrolidone carboxylate into the PC_1 system. In summary, PC_1Z_2 exhibited excellent physicochemical properties.

3.3. Photothermal antibacterial effect evaluation of PC_1Z_2 sponges

The broad-spectrum antibacterial properties of wound dressings are crucial for improving the prognosis of infected wounds [29]. Upon NIR laser irradiation for 10 min, the water temperature surrounding the PC_1Z_2 sponge increased from 26.5 to 50 °C, as depicted in Fig. 3A and E. The photothermal efficacy of the PC_1Z_2 sponge remained consistent even after multiple heating and cooling cycles, as illustrated in Fig. 3B. Escherichia coli and Staphylococcus aureus were used as model bacterial strains to assess the antibacterial efficacy of the PC_1Z_2 sponge. The antibacterial effect was quantified using the plate count method, and morphological alterations were observed under a microscope. Without NIR irradiation, the PC_1Z_2 group exhibited viable Staphylococcus aureus and E. coli, with inhibition rates of 72.4 ± 2.3 % and 70.6 ± 3.5 %, respectively, as shown in Fig. 3C and D. Both PC_1 and PC_1Z_2 exhibited a certain degree of antibacterial effect without NIR irradiation. This can be attributed to the high specific surface area and adsorption capacity of CNTs, which enables them to capture bacteria. Additionally, the excellent electrical conductivity of CNTs may facilitate electron transfer with bacterial cell membranes, leading to an imbalance in the membrane potential and disruption of the energy metabolism of the bacteria. Furthermore, the surface of CNTs can generate reactive oxygen species (ROS), such as superoxide anions (O_2^-), hydroxyl radicals (•OH), and hydrogen peroxide (H_2O_2). ROS can damage bacterial cell membranes, proteins, and DNA [30,31]. However, these antibacterial effects are insufficient to completely kill bacteria, necessitating NIR photothermal therapy to further enhance the antibacterial rate. Following NIR irradiation, minimal viable bacteria were detected in the PC_1Z_2 group (Fig. 3F), with inhibition rates significantly increasing to 97.2 ± 2.4 % for Staphylococcus aureus and 96.3 ± 2.1 % for E. coli (Fig. 3G). The morphological changes in the bacteria after NIR irradiation were observed using SEM. E coli and S. aureus exhibited smooth and intact cell membranes in the blank control group. In contrast, the PC_1Z_2 group showed severe wrinkling and cytoplasmic leakage (Fig. 3I), likely due to the rapid temperature elevation in the PC_1Z_2 system post-NIR irradiation. This process induces electron transfer, producing superoxide and hydroxyl radicals, and the breakdown of endogenous water into highly cytotoxic singlet oxygen, leading to a substantial disruption of bacterial cell integrity [31]. To demonstrate the lethality of the PC_1Z_2 group against bacteria, live/dead staining kits were used to stain bacteria in sponges after NIR irradiation. As shown in Fig. 3J, the control and commercial CS groups exhibited widespread green fluorescence, indicating that the bacteria remained alive in these groups. However, PC_1 and PC_1Z_2 displayed significant areas of red fluorescence with a dramatic increase in the death of both Staphylococcus aureus and E. coli, directly demonstrating the enhanced photothermal ablation effect of the CNT-based material. The fluorescence quantification results (Fig. 3H) further support this conclusion.

The exceptional photothermal conversion capability of carbon nanotube sponges under near-infrared light suggests a plausible antibacterial mechanism: The extensive surface area of carbon nanotubes facilitates robust adsorption onto bacterial surfaces through van der Waals forces and electrostatic interactions [32]. This interaction impedes normal bacterial metabolism and growth by obstructing nutrient access and expelling metabolic waste, thereby promoting bacterial death. Additionally, carbon nanotubes demonstrate efficient photothermal conversion properties that, under specific conditions, such as light exposure or interaction with certain substances, can generate reactive oxygen species (ROS), including superoxide anion radicals, hydroxyl radicals, and hydrogen peroxide. These ROS exhibit potent oxidative characteristics capable of damaging biomacromolecules within bacterial cells, including lipids, proteins, and DNA, leading to structural and functional impairments in cells, thus achieving antibacterial effects [10]. The PC_1Z_2 sponge, which incorporates Zn^{2+} with inherent antibacterial and anti-inflammatory properties, gradually releases these metal ions into the surrounding milieu. These ions can interact with enzymes, proteins, and other biomolecules within bacterial cells, disrupting normal bacterial metabolism and physiological functions, thereby impeding bacterial growth and proliferation [33].

3.4. Biocompatibility and anti-inflammatory properties of the scaffolds

Cell migration is the movement of cells in response to migratory or chemical stimuli such as cytokines. The wound scratch assay replicates the cell migration behavior observed during in vivo wound healing [34]. In this study, HUVECs and L929 cells in the PC_1Z_2 group demonstrated the highest migration rates, with nearly confluent cells on both sides after 48 h. Compared to the control group, the migration distances of HUVECs and L929 cells in the PC_1Z_2 group were significantly increased at 24 and 48 h ($p < 0.05$). These findings highlight the significant enhancement in cell migration facilitated by the PC_1Z_2 scaffold loaded with l-pyrrolidone carboxylic acid zinc, underscoring its potential importance in advancing diabetic wound healing research. Cell viability was assessed using a Calcein-AM/PI dual-staining kit to visualize the distribution of live and dead cells in the various extracts. Following a 24 h incubation period with the extracts, HUVECs (Fig. 4G) and L929 cells (Fig. 4H) displayed robust growth and well-spread morphology. After 72 h of co-culture, HUVECs (Fig. 4C) and L929 cells (Fig. 4Q) in the PC_1Z_2 group exhibited notably increased fluorescence intensity, which was significantly different from that in the PC_1 and control groups ($p < 0.01$). These results validated the exceptional biocompatibility of the scaffolds and indicated that the PC_1Z_2 group effectively enhanced cell proliferation. During angiogenesis, blood vessel formation is tightly regulated by a delicate balance between positive and negative factors. Vascular endothelial growth factor (VEGF) plays a pivotal role in

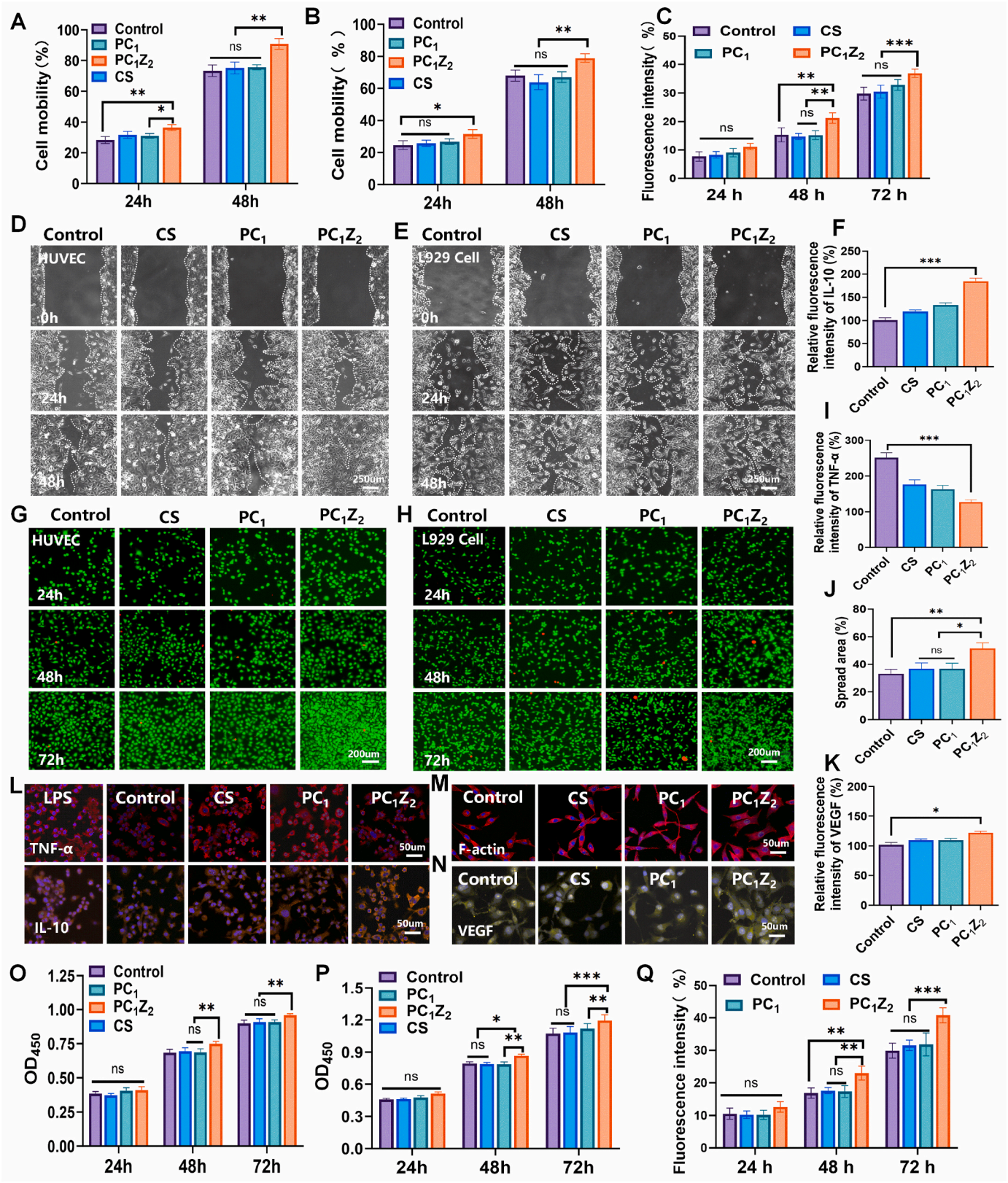

Fig. 4. Evaluation of biocompatibility and anti-inflammatory activity of sponges. (A) HUVECs migration rate. (B) L929 cell migration rate. (C) Quantification of live/dead fluorescence intensity in HUVECs. (D) HUVEC scratch assay. (E) L929 cell scratch assay. (F) IL-10 relative fluorescence intensity. (G) Live/dead cell staining images of HUVECs. (H) Live/dead cell staining images of L929 cells. (I) TNF-α relative fluorescence intensity via immunofluorescence staining. (J) L929 cell spreading area based on cytoskeleton staining. (K) VEGF relative fluorescence intensity via immunofluorescence staining. (L) TNF-α and IL-10 fluorescence staining in macrophage images. (M) Phalloidin fluorescence staining of L929 cell. (N) VEGF fluorescence staining images of HUVECs. (O) CCK-8 assay quantification for HUVECs. (P) CCK-8 assay quantification for L929 cells. (Q) Quantification of live/dead fluorescence intensity in L929 cells. ($*p < 0.05$, $**p < 0.01$, $***p < 0.001$).

orchestrating this process [35]. In vitro studies using normal human umbilical vein endothelial cells (HUVECs) revealed basal VEGF expression. However, co-culturing these cells with the PC_1Z_2 scaffold led to a significant increase in VEGF fluorescence (138.1 ± 3.5 %), indicating the potential of the scaffold to enhance angiogenesis ($p < 0.001$). This effect is likely mediated by Zn^{2+} release, which may promote endothelial migration. Fluorescent cytoskeleton staining revealed that L929 cells in the PC_1Z_2 group exhibited superior interconnection and stretching capabilities compared to those in the other groups. Furthermore, cells exposed to PC_1Z_2 extracts displayed the largest spreading area, suggesting that the scaffold effectively promoted cell adhesion and spreading.

A macrophage inflammation model was used to evaluate the scaffolds' anti-inflammatory properties [36]. As shown in Fig. 4L, TNF-α expression in macrophages was weak in the control group. In contrast, after LPS induction, RAW264.7 macrophages exhibited significant changes in size and morphology, with prominent pseudopodia, and TNF-α fluorescence expression reached the highest level 247.3 ± 5.1 %. IL-10 fluorescence expression was the lowest 98 ± 2.7 %. When macrophages were co-cultured with the PC_1Z_2 scaffold, TNF-α fluorescence expression was significantly reduced to 125 ± 4.1 % (Fig. 4I), whereas IL-10 expression was significantly increased to 187 ± 4.2 % (Fig. 4F) ($p < 0.05$). These results indicate that the PC_1Z_2 sponge exhibits notable in vitro anti-inflammatory activity. Compared with the PC_1 and control groups, the PC_1Z_2 group exhibited superior in vitro anti-inflammatory and pro-angiogenic properties, which could be attributed to the presence of Zn^{2+} in the culture medium [37]. The cells were exposed to the material extract solution, and their optical density (OD) was assessed using the CCK-8 method over 3 days. The OD values for all the groups notably increased over time. After 24 h of exposure to the extract, a statistically significant difference was observed between the PC_1Z_2 and control groups ($p < 0.05$). After 72 h of co-culture, the OD value of the PC_1Z_2 group significantly surpassed that of the other groups ($p < 0.05$), indicating the non-cytotoxicity of the sponges across all groups. Furthermore, PC_1Z_2 facilitated the growth and proliferation of HUVECs (Fig. 4O) and L929 cells (Fig. 4P) in vitro. These findings suggest that the PC_1Z_2 sponge demonstrates favorable biocompatibility and enhances the proliferation and migration of HUVECs and L929 cells while exhibiting anti-inflammatory properties.

3.5. In vitro hemostatic performance evaluation

Wound healing is a multifaceted process involving hemostasis, inflammation, and tissue remodelling. Patients with diabetes may

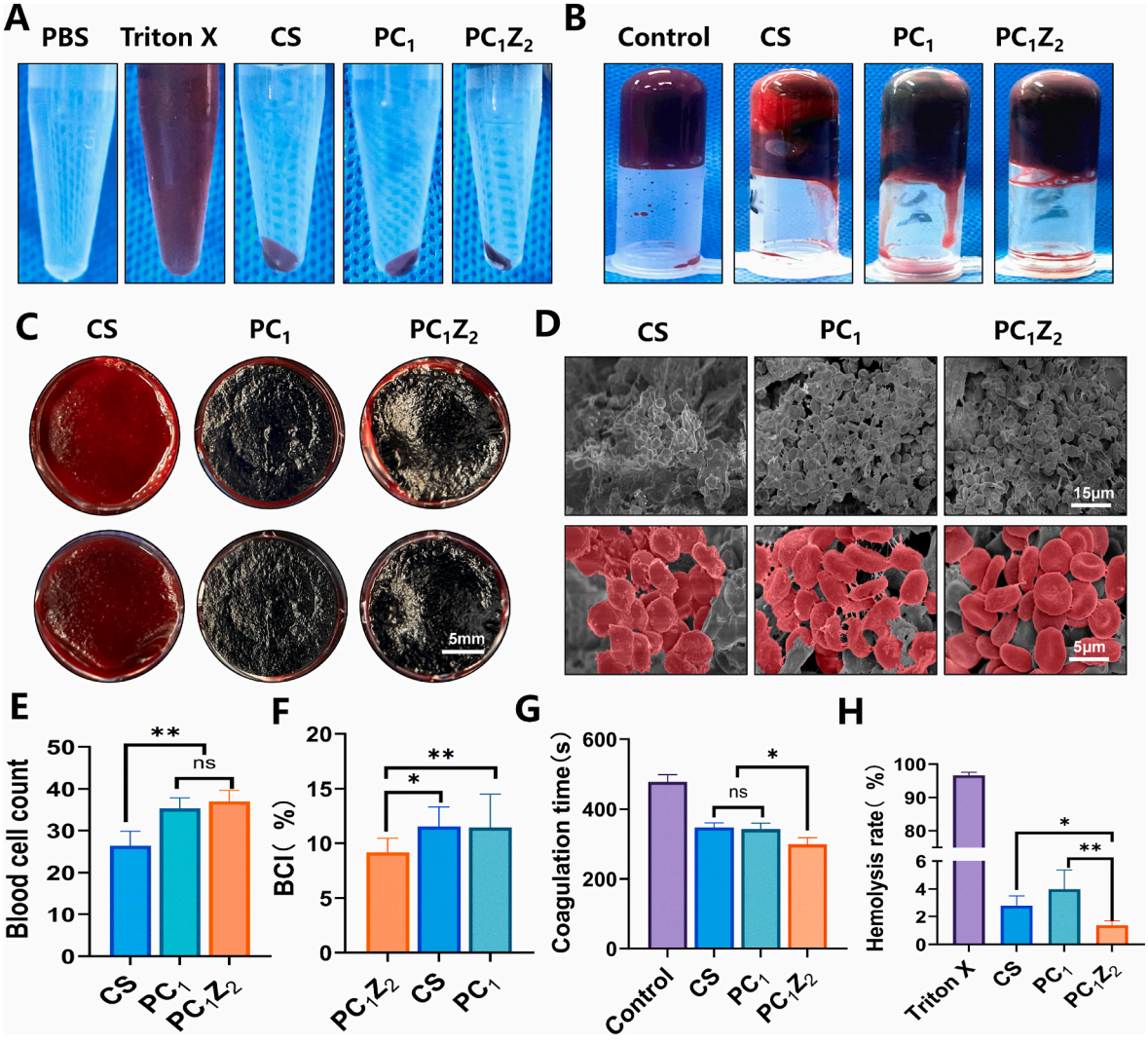

Fig. 5. In vitro assessment of sponge hemostatic performance. (A) The hemolysis rate is depicted in a representative sponge image. (B) The in vitro coagulation process is illustrated using representative images of the sponges. (C) Macroscopic images of sponges incubated with anticoagulant-treated whole blood. (D) Microscopic images of sponges incubated with anticoagulant-treated whole blood. (E) Quantitative analysis of blood cell adhesion. (F) Coagulation index. (G) Coagulation time. (H) Hemolysis rate. (*$p < 0.05$, **$p < 0.01$, ***$p < 0.001$).

experience reduced coagulation factor levels and impaired blood flow, necessitating external hemostatic interventions. [38]. As depicted in Fig. 5A, all tested sponges exhibited minimal hemolysis rates compared to the control group, with the PC_1Z_2 group demonstrating the lowest hemolysis rate of 1.4 ± 0.21 % (Fig. 5H). As shown in Fig. 5B, in vitro coagulation assays revealed that the PC_1Z_2 group exhibited robust clot formation, whereas the PC_1 and CS groups displayed incomplete blood coagulation. Furthermore, the coagulation time was significantly shorter in the PC_1Z_2 group (Fig. 5G) ($p < 0.05$). This superior performance can be attributed to the porous and loose structure of the PC_1Z_2 sponge, which enables the absorption of large volumes of blood and the concentration of coagulation factors, blood cells, and platelets [39]. Consequently, this structure promotes platelet adhesion and aggregation, forming a platelet plug that effectively halts blood loss from the wound. These sponges also release pertinent factors from both the intrinsic and extrinsic coagulation pathways, facilitating the formation of a stable clot and aiding in the management of wound hemorrhage. The large surface area of carbon nanotubes enhances their hemostatic performance by promoting the accelerated absorption of plasma water, leading to the concentration and activation of coagulation factors [40]. Fig. 5C illustrates that the immersion of sponges in whole blood, clot formation, and subsequent washing with PBS revealed the superior ability of the PC_1Z_2 sponge to entrap the blood cells. In the anticoagulant assays (Fig. 5D), all sponge groups exhibited blood cell adhesion, with the PC_1Z_2 group displaying denser adhesion in fresh whole-blood samples. Blood cell count confirmed a significantly higher accumulation of blood cells in the PC_1Z_2 sponge group (Fig. 5E) ($p < 0.01$). The coagulation index of the PC_1Z_2 group (9.57 ± 0.42 %) was lower than that of the PC_1 group (8.76 ± 0.71 %) and CS group(8.24 ± 0.35 %), with statistically significant differences (Fig. 5F)($p < 0.01$). Collectively, these results show that the PC_1Z_2 sponge displays enhanced hemostatic characteristics, surpassing those of other cohorts, likely owing to its efficient blood cell adhesion, increased concentration of coagulation factors, and prompt establishment of a durable clot.

3.6. In vivo hemostatic performance

Hemostatic sponges, characterized by their fine porous structure and positive charge, interact with platelets in the blood, accelerate thrombus formation, and effectively seal wounds for prompt hemostasis. The hemostatic performance of the PC_1Z_2 sponge was assessed using a rat tail amputation bleeding model. The results demonstrated that the PC_1Z_2 sponge outperformed simple gauze by absorbing exuded blood and securely trapping it within its pores, achieving adequate hemostasis (Fig. 6A). Additionally, the PC_1Z_2 sponge group exhibited significantly reduced blood loss (Fig. 6C) and shorter hemostasis time (Fig. 6D) than the gauze and CS groups ($p < 0.05$). We used a rat liver injury bleeding model to compare the hemostatic efficacy of the experimental sponges with that of a control group for visceral injuries. Fig. 6B shows representative images of the hemostasis process. Statistical analysis revealed that blood loss in the PC_1Z_2 and PC_1 sponge groups was 0.23 ± 0.03 g and 0.25 ± 0.04 g, respectively, with corresponding hemostasis times of 92 ± 5 s and 112 ± 4 s. In contrast, the control group exhibited higher blood loss (0.52 ± 0.04 g) and longer hemostasis time (130 ± 6 s), which were statistically significant(Fig. 6E and F) ($p < 0.01$). Furthermore, we investigated the hemostatic mechanism by analyzing scanning electron microscopy (SEM) images depicting the interactions between blood cells and hemostatic agents. As illustrated in Fig. 6G, the PC_1Z_2 group exhibited a notable presence of scattered blood cells on the sponge surface, demonstrating pronounced deformation (extension of pseudopodia) or aggregation compared with the CS and gauze control groups. These observations suggest the activation of blood cells and initiation of the coagulation process [41].

3.7. Evaluation of diabetic wound healing

Photothermal therapy (PTT) involves the use of photothermal agents to convert NIR laser energy into heat. This therapy, effective at a temperature of approximately 45 °C, induces vasodilation, enhances blood circulation, boosts metabolism, improves tissue nutrition, and reduces inflammation, making it a promising treatment for chronic wounds [42]. PTT also increases capillary permeability, facilitates exudate absorption, and reduces local tissue edema [43]. Furthermore, it aids in softening the scar tissue and inhibiting scar formation. To evaluate the effects of PC_1Z_2 scaffolds on cell proliferation, migration, and anti-inflammatory responses in vivo, we established a full-thickness diabetic wound model. Subsequently, NIR laser stimulation was administered to diabetic rat wounds covered with a sponge scaffold, and infrared thermography was used to assess the photothermal conversion efficacy of the various composite scaffolds. Following a 10 min NIR laser exposure, the temperature surrounding the PC_1Z_2 scaffold notably increased to 47.5 °C, as depicted in Fig. 7A. The progression of full-thickness skin wound healing on postoperative days 0, 7, 14, and 21 is shown in Fig. 7C. No significant infections were observed during mending. By day 3, the wounds in the control group exhibited persistent moisture, incomplete scab formation, and yellow exudates. Conversely, the CS, PC_1, and PC_1Z_2 groups displayed notably drier and scabbed wounds, likely attributable to the sponge's exceptional water absorption characteristics, which facilitated secretion absorption and maintained wound dryness [44]. By day 14, a substantial reduction in the wound area was evident across all groups compared to day 7, with the PC_1Z_2 group demonstrating nearly complete wound closure. The wounds treated with PC_1 also exhibited considerable closure, whereas the CS and control groups exhibited significantly larger wound areas. A schematic representation of the healing process at distinct time points in each group is shown in Fig. 7B. Consistent with qualitative observations, quantitative findings further substantiated that the wound closure rate in the PC_1Z_2 group surpassed that in the PC_1 and control groups ($p < 0.01$), underscoring the enhanced wound healing conferred by zinc pyrrolidone carboxylate. By day 21, the regenerated skin tissue in the PC_1Z_2 group displayed a diminished scar area.

Histopathological analysis using H&E (Fig. 7E) and Masson's trichrome staining (Fig. 7F) revealed that wounds in the PC_1 and PC_1Z_2 groups underwent re-epithelialization and granulation tissue formation during the remodelling phase. In contrast, the CS and control groups exhibited a delayed healing. Across all groups, the wound length decreased gradually as healing progressed, accompanied by increased granulation tissue thickness. Remarkably, the PC_1Z_2 group demonstrated the most significant trends. By day 7, minimal new tissue was observed in the control and CS groups, whereas the PC_1 group showed well-progressing granulation tissue healing, and the PC_1Z_2 group exhibited abundant granulation tissue healing. Statistical analysis of wound length supported the H&E staining findings (Fig. 7G), with the PC_1Z_2 group demonstrating a significantly shorter wound length than the other groups ($p < 0.05$), followed by the PC_1, CS, and control groups. Similar trends were observed on days 14 and 21, with the PC_1Z_2 group showing the shortest wound length. Compared to the control group, the PC_1Z_2 group displayed significantly thicker granulation tissue (Fig. 7H) and exhibited higher levels of well-organized collagen deposition (Fig. 7I). Furthermore, by day 21, the PC_1Z_2 group exhibited newly formed granulation tissue and more intricate epidermal structures than the other groups.

Angiogenesis is critical for tissue repair, as it facilitates blood flow and delivers oxygen and nutrients to support tissue restructuring [45]. In this study, we used CD31 as a marker for endothelial cells to investigate vascular development during wound healing. The results (Fig. 7D) demonstrated a substantial increase in CD31 expression in the PC_1Z_2 group, leading to a more extensive distribution and larger blood vessel diameter. These differences were statistically significant, as confirmed by fluorescence quantification analysis (Fig. 7J)($p < 0.05$). These

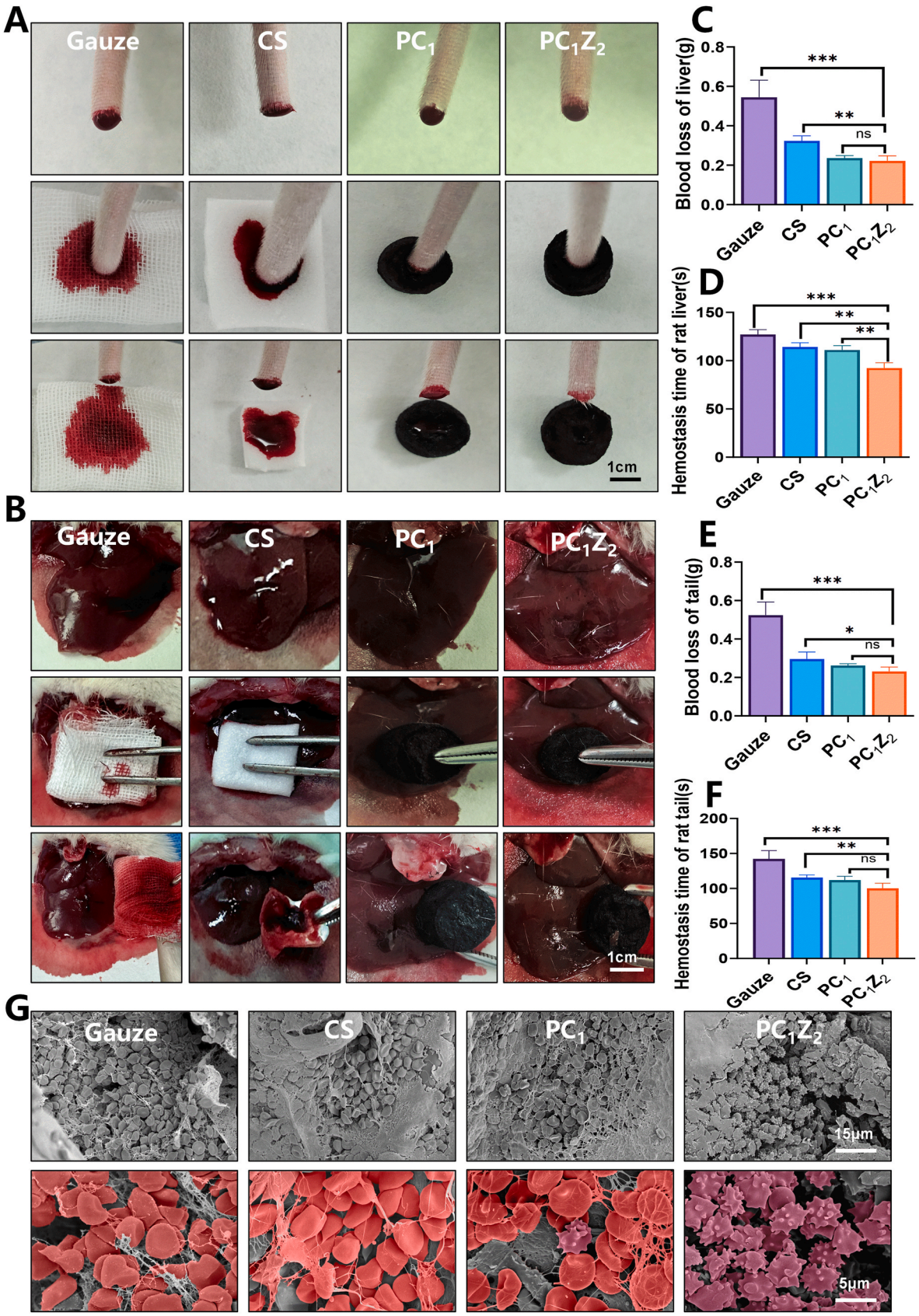

Fig. 6. Sponges were applied to the rat tails and liver for hemostasis. (A) Representative images of the hemostasis process in rat tail amputation. (B) Representative images of hemostasis in the rat liver injury model. (C) Blood loss in the liver injury model. (D) Hemostasis time in the liver injury model. (E) Blood loss in the tail amputation model. (F) Hemostasis time in the tail amputation model. (G) Microscopic images of sponge post-hemostasis. ($^{*}p < 0.05$, $^{**}p < 0.01$, $^{***}p < 0.001$).

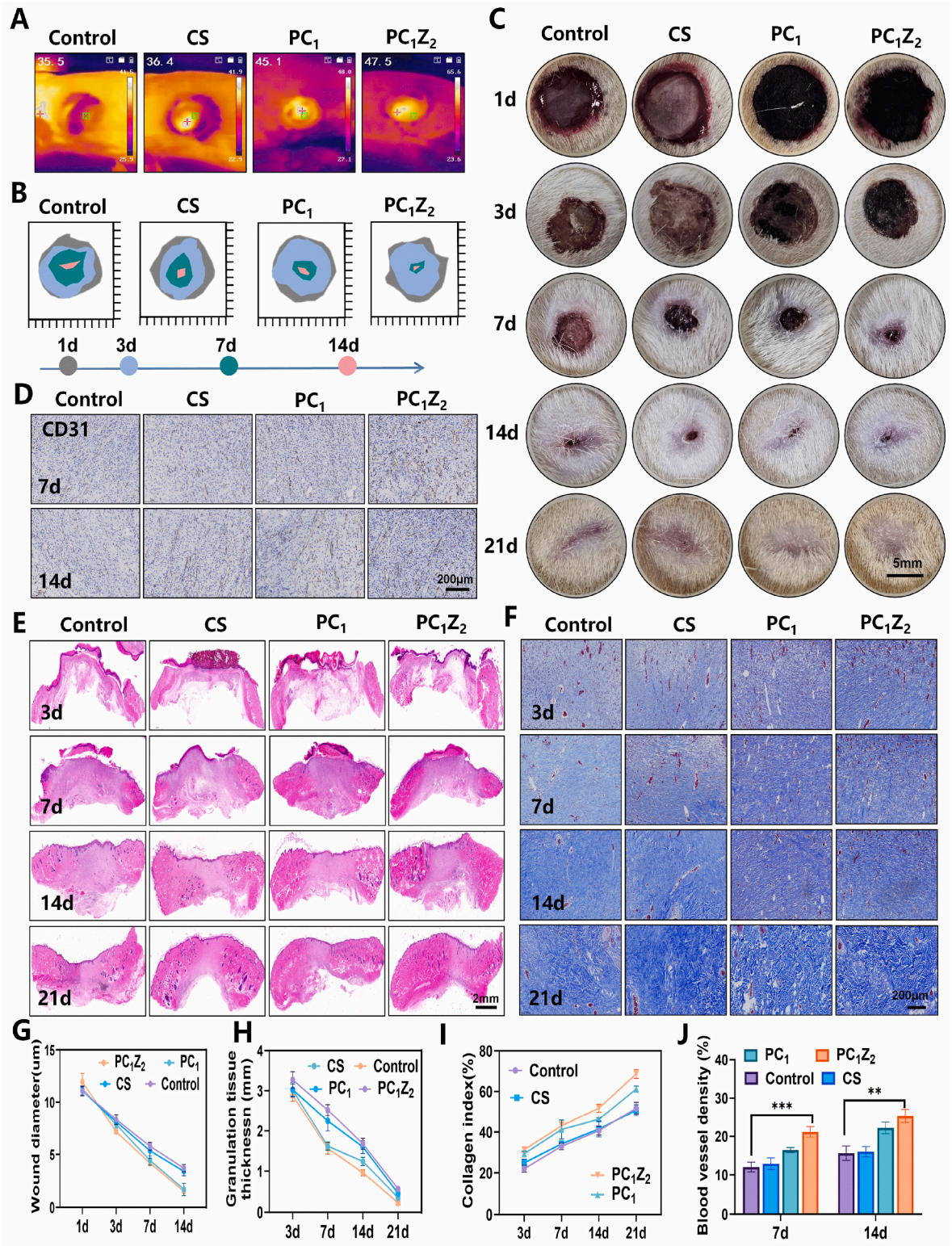

Fig. 7. Sponge Treatment of Diabetic Wounds in Rats. (A) Thermal image of a rat wound. (B) Schematic illustration of the dynamic healing process. (C) Progression photos showing wound healing at various time points. (D) Immunohistochemistry images of CD31. (E) H&E staining images. (F) Images of Masson's trichrome staining. (G) Measurement of wound diameter. (H) Assessment of granulation tissue thickness. (I) Calculation of collagen index. (J) Quantitative analysis of vessel count from Masson's staining. (*$p < 0.05$, **$p < 0.01$, ***$p < 0.001$).

findings demonstrate that PC_1Z_2 possesses outstanding photothermal conversion efficiency, significantly accelerates diabetic wound healing with reduced healing time, and effectively mitigates scar hypertrophy.

3.8. Histological analysis

Chronic wound healing is hindered by persistent chronic inflammation, particularly in diabetic chronic wounds, where research

suggests that the inflammatory phase may be disrupted, thereby delaying the progression to the proliferative phase. Macrophages are crucial early responders to inflammation and play a key role in recognizing tissue damage and coordinating repair processes [46]. Initially, macrophages exhibit a pro-inflammatory (M1) phenotype, which then transitions to an anti-inflammatory (M2) phenotype to support tissue repair and advance healing [47]. However, in diabetic wounds, this transition is disrupted, leading to an abnormal shift of macrophages from the inflammatory (M1) to anti-inflammatory (M2) state, ultimately impeding the wound healing process. Interestingly, tissues treated with sponges showed the most significant inflammatory response on day 3, which gradually decreased by day 7 (Fig. 8A).

The TNF-α-positive area varied among the groups, being the highest in the control group, followed by the PADM sponge and CS sponge groups, and lowest in the PC_1Z_2 sponge group (Fig. 8B). Conversely, the IL-10 positivity results displayed an inverse pattern (Fig. 8C), with the PC_1Z_2 group showing the highest expression, followed by the PC_1 and CS sponge groups. In contrast, the control group exhibited the lowest levels of these proteins (Fig. 8D) ($p < 0.01$). Early inflammatory responses are essential for clearing dead cells, bacteria, and harmful substances, removing tissue necrosis, and creating a conducive environment for subsequent proliferation. However, excessive inflammation during the later stages of wound healing can lead to the formation of scars. Therefore, the PC_1Z_2 sponge initiates an inflammatory response and demonstrates significant anti-inflammatory effects during the granulation tissue and tissue remodelling phases, which is crucial for enhancing diabetic wound healing. Ki67 is a vital cell proliferation marker that is commonly used to evaluate wound healing [8]. The findings depicted in Fig. 8E indicate a gradual decrease in the intensity and area of Ki67-positive staining from days 14 to 21 in all groups, reflecting the ongoing wound repair process. Notably, the PC_1Z_2 group consistently exhibited a significantly higher Ki67-positive staining intensity than the other three groups at all time points (Fig. 8F) ($p < 0.01$), suggesting a heightened level of cell proliferation in the PC_1Z_2 group during the

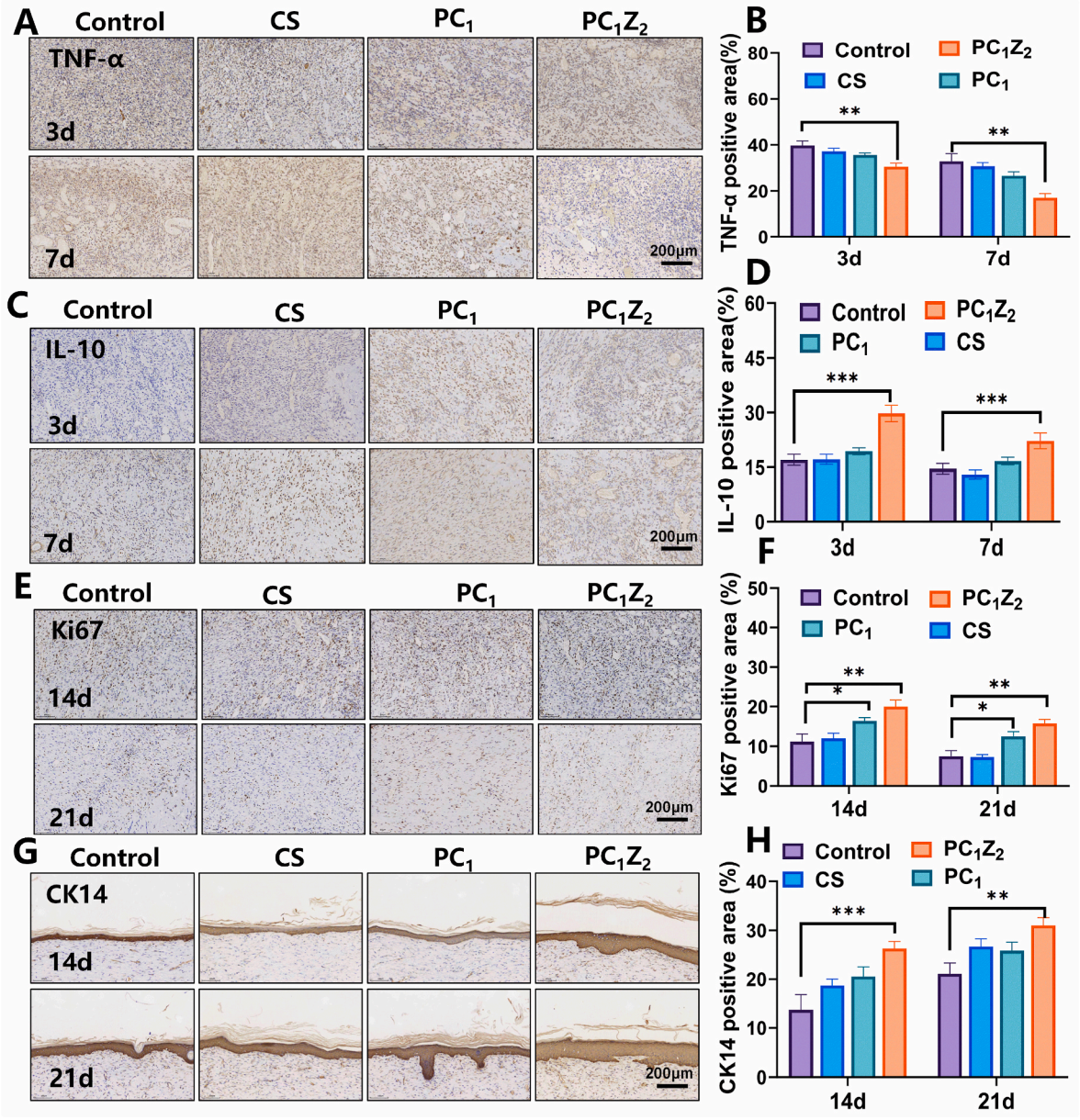

Fig. 8. Immunohistochemical analysis. (A) TNF-α immunohistochemical staining images. (B) Quantitative analysis of TNF-α area. (C) IL-10 immunohistochemical staining images. (D) Quantitative analysis of IL-10 area. (E) Ki67 immunofluorescence staining images. (F) Quantitative analysis of IL-10 area. (G) CK14 immunohistochemical staining images. (H) Quantitative analysis of CK14 area. (*$p < 0.05$, **$p < 0.01$, ***$p < 0.001$).

phases of tissue remodelling and re-epithelialization, in contrast to the control group. Cytokeratin (CK) is an important biomarker associated with epidermal differentiation and re-epithelialization. CK14, a type I intermediate filament keratin, combines with type II keratin CK5 to form basal keratin filaments within squamous epithelial cells [12]. Immunohistochemical analysis of CK14 consistently displayed robust CK14 expression in the regenerated epithelium across all time points in the PC_1Z_2 and PC_1 groups, which was more pronounced in the PC_1Z_2 group (Fig. 8G and H). These findings validated the enhanced and expedited re-epithelialization of the wound tissue in the PC_1 and PC_1Z_2 groups compared to that in the control group, with the PC_1Z_2 group exhibiting superior regenerative properties. These results were consistent with the histological results of hematoxylin and eosin staining. Accelerated wound closure, epithelial cell proliferation, angiogenesis, collagen synthesis, and other findings collectively support the exceptional therapeutic efficacy of the 3D carbon nanotube sponge combined with pyrrolidone carboxylic acid zinc. Hence, customizable optoelectronic integrated scaffolds show promising prospects for advancing chronic wound healing and may represent a precise therapeutic approach for tissue regeneration.

3.9. Potential mechanisms

Tissue regeneration is a complex process characterized by intricate cellular and biochemical cascades that progress through four distinct yet partially overlapping phases: hemostasis, inflammation, proliferation, and tissue remodelling [1,3]. However, the coordination of these phases often fails during hemostasis owing to inadequate management of wound exudates and a lack of active coupling with endogenous electric fields, resulting in passive tissue repair that hinders the natural tissue cascade repair process [7,8]. To overcome these obstacles, a PC_1Z_2 sponge scaffold was developed to efficiently manage excessive exudate, transmit bioelectric signals, and align with the tissue repair cascade for precise tissue remodelling. The superior performance of the PC_1Z_2 scaffold in tissue repair can be attributed to its unique synergistic mechanism: (1) Simulating the extracellular matrix, the PC_1Z_2 sponge scaffold conveys chemical and mechanical signals to cells, promoting cell adhesion, proliferation, and ultimately, tissue repair and regeneration [22]. (2) Owing to its exceptional water absorption and retention capabilities, the PC_1Z_2 sponge effectively regulated wound exudates, creating an optimal micro-moist healing environment. Additionally, it concentrates and absorbs nutrients and growth factors from the surrounding tissues, facilitating cellular growth and tissue regeneration [48]. (3) The PC_1Z_2 optoelectronic properties enable it to effectively elevate the temperature of diabetic wounds under NIR laser exposure. This process triggers vasodilation, boosts blood circulation, enhances exudate absorption, reduces localized tissue edema, and accelerates tissue healing [29]. Furthermore, the photothermal therapy features of the sponge imparted antimicrobial property. Reactive ROS, such as superoxide anion radicals, hydroxyl radicals, and hydrogen peroxide, are produced upon exposure to light or specific substances. These ROS exhibit potent oxidative properties that target bacterial cell biomacromolecules, disrupt cellular structure and function, and exert antibacterial effects [31,32]. (4) The porous and airy structure of the PC_1Z_2 sponge enables it to absorb large volumes of blood and concentrate coagulation components, red blood cells, and platelets. This promotes platelet adhesion, aggregation, and activation, leading to thrombus formation and halting blood flow from the wound. Additionally, the extensive surface area of carbon nanotubes accelerates moisture absorption from the plasma and concentrates and activates coagulation factors, thereby enhancing the hemostatic performance [39,41]. (5) The PC_1Z_2 sponge, in conjunction with the absorption of wound exudates, gradually releases Zn^{2+} ions, thereby augmenting the recruitment of immune cells and cytokines to the wound site. This mechanism downregulates the expression of pro-inflammatory cytokines, thereby abbreviating the inflammatory phase and fostering a more conducive environment for tissue regeneration [36,37]. (6) Following the absorption of wound exudates, the PC_1Z_2 sponge actively interfaces with endogenous electric fields, thereby transmitting intrinsic bioelectric signals to the wound site. Guided by these endogenous electrical cues, fibroblasts proliferate and secrete collagen, promoting granulation tissue formation. Endothelial cells expedite migration and vascularization, whereas keratinocytes proliferate and enhance keratin expression, facilitating re-epithelialization. This synergistic cascade of events effectively harmonizes with the intricate process of tissue remodelling post-injury, promoting efficient tissue repair and regeneration [44,49].

4. Conclusion

In this study, we developed a novel photothermal electroactive sponge scaffold, PC_1Z_2, characterized by superior water absorption and electrical conductivity. This scaffold, designed to mimic the extracellular matrix microenvironment, modulates immune responses in chronic diabetic wounds via the gradual release of Zn^{2+} ions. The scaffold generates micro-negative pressure on the wound surface, enhancing exudate and blood absorption for rapid hemostasis in patients with diabetes mellitus. Upon interaction with biological fluids, the scaffold, possessing high cell/tissue affinity, efficiently delivers endogenous electric fields to cells and tissues, boosting cellular metabolic activity crucial for wound healing. Validation in a diabetic wound model demonstrated early exudate collection, bioelectric signal transmission, and active coordination of tissue repair processes for precise tissue remodelling. Additionally, the antimicrobial properties of sponge scaffolds can be enhanced by photothermal conversion, expediting granulation tissue formation, collagen deposition, and re-epithelialization. In summary, this photothermal electroactive sponge dressing offers a novel strategy for diabetic wound repair by combining hemostatic, anti-inflammatory, antimicrobial, and wound-healing properties.

CRediT authorship contribution statement

Chenwei Wu: Writing – original draft, Visualization, Resources, Project administration, Methodology, Investigation, Formal analysis, Data curation, Conceptualization. **Bo Liu:** Writing – review & editing, Writing – original draft, Visualization, Validation, Supervision, Software, Funding acquisition, Formal analysis. **Qiulan Wen:** Writing – original draft, Validation, Supervision, Software, Resources, Project administration, Methodology, Investigation, Formal analysis, Data curation, Conceptualization. **Qiliang Zhai:** Writing – review & editing, Writing – original draft, Investigation, Funding acquisition, Formal analysis.

Availability of data and materials

All data generated or analyzed during this study are included in this article.

Ethics approval and consent to participate

All animal experiments were approved by the Animal Ethics Committee of Nanfang Hospital of Southern Medical College (IACUC-LAC-20241225-003, Guangzhou, China) and were conducted in accordance with the National Research Council Guide for the Care and Use of Laboratory Animals.

Consent for publication

All authors have been sent for publication.

Funding

This study was financially supported by the Jiangxi Provincial Science and Technology Agency Project (20242BAB20423), National Natural Science Foundation of China (No. 82360598), and Ganzhou Municipal Science and Technology Project (No. 2023NS127390). Guangxi Key Laboratory of Orthopedic Biomaterials Research and Development and Clinical Transformation(lgy20201208). Guangxi Medical and Health Key Discipline Construction Project (QZDXK202202). The authors acknowledge the contributions of this study.

Declaration of competing interest

We declare that no conflict of interest exits in the submission of this manuscript, and manuscript is approved by all authors for publication. I would like to declare on behalf of my co-authors that the work described was original research that has not been published previously, and not under consideration for publication elsewhere, in whole or in part. All the authors listed have approved the manuscript that is enclosed.

Appendix A. Supplementary data

Supplementary data to this article can be found online at https://doi.org/10.1016/j.mtbio.2025.101769.

Data availability

Data will be made available on request.

References

[1] M. Sharifiaghdam, E. Shaabani, R. Faridi-Majidi, S.C. De Smedt, K. Braeckmans, J. C. Fraire, Macrophages are therapeutic targets for promoting diabetic wound healing, Mol. Ther. 30 (9) (2022 Sep 7) 2891–2908, https://doi.org/10.1016/j.ymthe.2022.07.016. Epub 2022 Aug 2. PMID: 35918892; PMCID: PMC9482022.

[2] F.X. Yu, P.S.Y. Lee, L. Yang, N. Gao, Y. Zhang, A.V. Ljubimov, E. Yang, Q. Zhou, L. Xie, Sensory neuropathy and inflammation impact epithelial wound healing in diabetic corneas, Prog. Retin. Eye Res. 89 (2022 Jul) 101039, https://doi.org/10.1016/j.preteyeres.2021.101039. Epub 2022 Jan 4. PMID: 34991965; PMCID: PMC9250553.

[3] A. Uberoi, A. McCready-Vangi, E.A. Grice, The wound microbiota: microbial mechanisms of impaired wound healing and infection, Nat. Rev. Microbiol. 22 (8) (2024 Aug) 507–521, https://doi.org/10.1038/s41579-024-01035-z. Epub 2024 Apr 4. PMID: 38575708.

[4] F. Du, M. Liu, J. Wang, L. Hu, D. Zeng, S. Zhou, L. Zhang, M. Wang, X. Xu, C. Li, J. Zhang, S. Yu, Metformin coordinates with mesenchymal cells to promote VEGF-mediated angiogenesis in diabetic wound healing through Akt/mTOR activation, Metabolism 140 (2023 Mar) 155398, https://doi.org/10.1016/j.metabol.2023.155398. Epub 2023 Jan 7. PMID: 36627079.

[5] R. Luo, J. Dai, J. Zhang, Z. Li, Accelerated skin wound healing by electrical stimulation, Adv. Healthcare Mater. 10 (16) (2021 Aug) e2100557, https://doi.org/10.1002/adhm.202100557. Epub 2021 May 4. PMID: 33945225.

[6] X. Xu, H. Zhang, Y. Yan, J. Wang, L. Guo, Effects of electrical stimulation on the skin surface, Acta Mech. Sin. 37 (12) (2021) 1843–1871, https://doi.org/10.1007/s10409-020-01026-2. Epub 2021 Feb 6. PMID: 33584001; PMCID: PMC7866966.

[7] Y. Yan, Y. Chen, H. Dai, W. Zhang, R. Guo, Reconfiguring the endogenous electric field of a wound through a conductive hydrogel for effective exudate management to enhance skin wound healing, J. Mater. Chem. B 12 (44) (2024 Nov 13) 11347–11358, https://doi.org/10.1039/d4tb01349b. PMID: 39499499.

[8] H. Zhou, L. Chen, C. Huang, Z. Jiang, H. Zhang, X. Liu, F. Zhu, Q. Wen, P. Shi, K. Liu, L. Yang, Endogenous electric field coupling Mxene sponge for diabetic wound management: haemostatic, antibacterial, and healing, J. Nanobiotechnol. 22 (1) (2024 Sep 2) 530, https://doi.org/10.1186/s12951-024-02799-5. PMID: 39218901; PMCID: PMC11367980.

[9] R. Luo, Y. Liang, J. Yang, H. Feng, Y. Chen, X. Jiang, Z. Zhang, J. Liu, Y. Bai, J. Xue, S. Chao, Y. Xi, X. Liu, E. Wang, D. Luo, Z. Li, J. Zhang, Reshaping the endogenous electric field to boost wound repair via electrogenerative dressing, Adv. Mater. 35 (16) (2023 Apr) e2208395, https://doi.org/10.1002/adma.202208395. Epub 2023 Mar 9. PMID: 36681867.

[10] R. Sridharan, B. Monisha, P.S. Kumar, K.V. Gayathri, Carbon nanomaterials and its applications in pharmaceuticals: a brief review, Chemosphere 294 (2022 May) 133731, https://doi.org/10.1016/j.chemosphere.2022.133731. Epub 2022 Jan 25. PMID: 35090848.

[11] L. Chen, S. Zeng, H. Zhang, Z. Jiang, H. Zhou, S. Yu, Q. Yu, M. Li, C. Huang, P. Shi, K. Liu, L. Yang, Synergistic effect of protein foams and polysaccharide on the invisible hemostasis of acellular dermal matrix sponges, Int. J. Biol. Macromol. 274 (Pt 2) (2024 Aug) 133138, https://doi.org/10.1016/j.ijbiomac.2024.133138. Epub 2024 Jun 18. PMID: 38901509.

[12] Li W, Zhang H, Chen L, Huang C, Jiang Z, Zhou H, Zhu X, Liu X, Zheng Z, Yu Q, He Y, Gao Y, Ma J, Yang L. Cell membrane-derived nanovesicles as extracellular vesicle-mimetics in wound healing. Mater Today Bio. 2025 Feb 18;31:101595. doi: 10.1016/j.mtbio.2025.101595. PMID: 40104636; PMCID: PMC11914519.L. Chen, Z. Jiang, H. Zhou, H. Zhang, C. Huang, Q. Wen, X. Liu, Y. He, P. Shi, K. Liu, L. Yang, Effect of hyaluronic acid on the formation of acellular dermal matrix-based interpenetrating network sponge scaffolds for accelerating diabetic wound healing through photothermal warm bath, Int. J. Biol. Macromol. 283 (Pt 1) (2024 Dec) Epub 2024 Nov 4. PMID: 39505193 137268, doi:10.1016/j.ijbiomac.2024.137268.

[13] Y. Peng, B. Guo, W. Wang, P. Yu, Z. Wu, L. Shao, W. Luo, Efficient preparation of nitrogen-doped lignin-based carbon nanotubes and the selectivity of nitrogen speciation for photothermal therapy, Int. J. Biol. Macromol. 238 (2023 May 31) 124127, https://doi.org/10.1016/j.ijbiomac.2023.124127. Epub 2023 Mar 21. PMID: 36958448.

[14] X. Li, L. Zhang, Z. Liu, R. Wang, T. Jiao, Recent progress in hydrogels combined with phototherapy for bacterial infection: a review, Int. J. Biol. Macromol. 274 (Pt 1) (2024 Aug) 133375, https://doi.org/10.1016/j.ijbiomac.2024.133375. Epub 2024 Jun 22. PMID: 38914386.

[15] A. López-Moreno, J. Villalva, E.M. Pérez, Mechanically interlocked derivatives of carbon nanotubes: synthesis and potential applications, Chem. Soc. Rev. 51 (23) (2022 Nov 28) 9433–9444, https://doi.org/10.1039/d2cs00510g. PMID: 36239532.

[16] M.A. Rosa, A. Granja, C. Nunes, S. Reis, A.B.S. da Silva, K.N.D.S. Leal, M.A. Z. Arruda, L.F. Gorup, M.G. Santos, M.V.S. Dias, E.C. Figueiredo, Magnetic carbon nanotubes modified with proteins and hydrophilic monomers: cytocompatibility, in-vitro toxicity assays and permeation across biological interfaces, Int. J. Biol. Macromol. 269 (Pt 1) (2024 Jun) 131962, https://doi.org/10.1016/j.ijbiomac.2024.131962. Epub 2024 Apr 29. PMID: 38692550.

[17] S. Sharmeen, A.F.M.M. Rahman, M.M. Lubna, K.S. Salem, R. Islam, M.A. Khan, Polyethylene glycol functionalized carbon nanotubes/gelatin-chitosan nanocomposite: an approach for significant drug release, Bioact. Mater. 3 (3) (2018 Apr 4) 236–244, https://doi.org/10.1016/j.bioactmat.2018.03.001. PMID: 29744462; PMCID: PMC5935779.

[18] W. Zhang, L. Zhao, C. Gao, J. Huang, Q. Li, Z. Zhang, Highly resilient, biocompatible, and antibacterial carbon nanotube/hydroxybutyl chitosan sponge dressing for rapid and effective hemostasis, J. Mater. Chem. B 9 (47) (2021 Dec 8) 9754–9763, https://doi.org/10.1039/d1tb01911b. PMID: 34796365.

[19] T. Li, Q. Wen, F. Zhu, Y. Hu, J. Gong, X. Zhang, C. Huang, H. Zhou, L. Chen, Y. Pan, A tranexamic acid-functionalized acellular dermal matrix sponge co-loaded with magnesium ions: enhancing hemostasis, vascular regeneration, and re-epithelialization for comprehensive diabetic wound healing, Biomater. Adv. 167 (2025 Feb) 214096, https://doi.org/10.1016/j.bioadv.2024.214096. Epub 2024 Oct 31. PMID: 39500149.

[20] F. Zhu, Q. Wen, Y. Hu, J. Gong, X. Zhang, C. Huang, H. Zhou, L. Chen, L. Yu, Chondroitin sulfate sponge scaffold for slow-release Mg2+/Cu2+ in diabetic wound management: hemostasis, effusion absorption, and healing, Int. J. Biol. Macromol. 282 (Pt 6) (2024 Dec) 137561, https://doi.org/10.1016/j.ijbiomac.2024.137561. Epub 2024 Nov 12. PMID: 39537068.

[21] L. Lan, J. Ping, H. Li, C. Wang, G. Li, J. Song, Y. Ying, Skin-inspired all-natural biogel for bioadhesive interface, Adv. Mater. 36 (25) (2024 Jun) e2401151, https://doi.org/10.1002/adma.202401151. Epub 2024 Apr 9. PMID: 38558183.

[22] Y. Li, J. Wang, D. Qian, L. Chen, X. Mo, L. Wang, Y. Wang, W. Cui, Electrospun fibrous sponge via short fiber for mimicking 3D ECM, J. Nanobiotechnol. 19 (1) (2021 May 8) 131, https://doi.org/10.1186/s12951-021-00878-5. PMID: 33964948; PMCID: PMC8106196.

[23] M. Zhou, J. Liao, G. Li, Z. Yu, D. Xie, H. Zhou, F. Wang, Y. Ren, R. Xu, Y. Dai, J. Wang, J. Huang, R. Zhang, Expandable carboxymethyl chitosan/cellulose nanofiber composite sponge for traumatic hemostasis, Carbohydr. Polym. 294 (2022 Oct 15) 119805, https://doi.org/10.1016/j.carbpol.2022.119805. Epub 2022 Jul 2. PMID: 35868765.

[24] W. Li, Z. Liu, X. Tan, N. Yang, Y. Liang, D. Feng, H. Li, R. Yuan, Q. Zhang, L. Liu, L. Ge, All-in-One self-powered microneedle device for accelerating infected diabetic wound repair, Adv. Healthcare Mater. 13 (13) (2024 May) e2304365, https://doi.org/10.1002/adhm.202304365. Epub 2024 Feb 14. PMID: 38316147.

[25] C. Lee, S. Lee, S.W. Kang, Enhanced porous membrane fabrication using cellulose acetate and citric acid: improved structural integrity, thermal stability, and gas permeability, Carbohydr. Polym. 324 (2024 Jan 15) 121571, https://doi.org/10.1016/j.carbpol.2023.121571. Epub 2023 Nov 7. PMID: 37985069.

[26] S. Yao, Y. Yang, C. Li, K. Yang, X. Song, C. Li, Z. Cao, H. Zhao, X. Yu, X. Wang, L. N. Wang, Axon-like aligned conductive CNT/GelMA hydrogel fibers combined with electrical stimulation for spinal cord injury recovery, Bioact. Mater. 35 (2024 Feb 22) 534–548, https://doi.org/10.1016/j.bioactmat.2024.01.021. PMID: 38414842; PMCID: PMC10897856.

[27] B. Behrouznejad, S.B. Sadat, E. Masaeli, The orchestration of sustained drug delivery by bacterial cellulose/gelatin nanocomposites reinforced with carboxylic carbon nanotubes, Carbohydr. Polym. 333 (2024 Jun 1) 121917, https://doi.org/10.1016/j.carbpol.2024.121917. Epub 2024 Feb 9. PMID: 38494242.

[28] Y. Tang, M. Si, Y.J. Wang, J. Zhou, Y. Deng, K. Xia, Z. Jiang, D. Zhang, S.Y. Zheng, J. Yang, Endocytosis-inspired zwitterionic gel tape for high-efficient and sustainable underoil adhesion, Adv. Sci. (Weinh.) 11 (42) (2024 Nov) e2407501, https://doi.org/10.1002/advs.202407501. Epub 2024 Sep 9. PMID: 39248332; PMCID: PMC11558084.

[29] X. Wei, C. Liu, Z. Li, Z. Gu, J. Yang, K. Luo, Chitosan-based hydrogel dressings for diabetic wound healing via promoting M2 macrophage-polarization, Carbohydr. Polym. 331 (2024 May 1) 121873, https://doi.org/10.1016/j.carbpol.2024.121873. Epub 2024 Jan 30. PMID: 38388059.
[30] W. Wang, F. Wu, Q. Zhang, N. Zhou, M. Zhang, T. Zheng, Y. Li, B.Z. Tang, Aggregation-induced emission nanoparticles for single near-infrared light-triggered photodynamic and photothermal antibacterial therapy, ACS Nano 16 (5) (2022 May 24) 7961–7970, https://doi.org/10.1021/acsnano.2c00734. Epub 2022 May 3. PMID: 35504042.
[31] A. Khalid, A. Madni, B. Raza, M.U. Islam, A. Hassan, F. Ahmad, H. Ali, T. Khan, F. Wahid, Multiwalled carbon nanotubes functionalized bacterial cellulose as an efficient healing material for diabetic wounds, Int. J. Biol. Macromol. 203 (2022 Apr 1) 256–267, https://doi.org/10.1016/j.ijbiomac.2022.01.146. Epub 2022 Jan 29. PMID: 35093443.
[32] Y. Liu, H. Liu, S. Guo, Y. Zhao, J. Qi, R. Zhang, J. Ren, H. Cheng, M. Zong, X. Wu, B. Li, A review of carbon nanomaterials/bacterial cellulose composites for nanomedicine applications, Carbohydr. Polym. 323 (2024 Jan 1) 121445, https://doi.org/10.1016/j.carbpol.2023.121445. Epub 2023 Sep 29. PMID: 37940307.
[33] G. Wu, F. Ma, Y. Xue, Y. Peng, L. Hu, X. Kang, Q. Sun, D.F. Ouyang, B. Tang, L. Lin, Chondroitin sulfate zinc with antibacterial properties and anti-inflammatory effects for skin wound healing, Carbohydr. Polym. 278 (2022 Feb 15) 118996, https://doi.org/10.1016/j.carbpol.2021.118996. Epub 2021 Dec 11. PMID: 34973799.
[34] A.A. Solbu, D. Caballero, S. Damigos, S.C. Kundu, R.L. Reis, Ø. Halaas, A.S. Chahal, B.L. Strand, Assessing cell migration in hydrogels: an overview of relevant materials and methods, Mater Today Bio 18 (2022 Dec 29) 100537, https://doi.org/10.1016/j.mtbio.2022.100537. PMID: 36659998; PMCID: PMC9842866.
[35] S.Y. Park, J.K. Lee, S.H. Lee, D.S. Kim, J.W. Jung, J.H. Kim, S.W. Baek, S. You, D. Y. Hwang, D.K. Han, Multifunctional vitamin D-incorporated PLGA scaffold with BMP/VEGF-overexpressed tonsil-derived MSC via CRISPR/Cas9 for bone tissue regeneration, Mater Today Bio 28 (2024 Sep 14) 101254, https://doi.org/10.1016/j.mtbio.2024.101254. PMID: 39328787; PMCID: PMC11426062.
[36] F. Shi, A. Ergashev, Z. Pan, H. Sun, L. Kong, Y. Jin, T. Zhang, Z. Liu, H. Xie, J. Wang, H. Li, Y. Wang, L. Zheng, J. Shen, A. Herrmann, G. Chen, H. Kong, Macrophage-mimicking nanotherapy for attenuation of acute pancreatitis, Mater Today Bio 30 (2024 Dec 15) 101406, https://doi.org/10.1016/j.mtbio.2024.101406. PMID: 39816666; PMCID: PMC11733200.
[37] B. Tao, C. Lin, X. Qin, Y. Yu, A. Guo, K. Li, H. Tian, W. Yi, D. Lei, Y. Chen, L. Chen, Fabrication of gelatin-based and Zn2+-incorporated composite hydrogel for accelerated infected wound healing, Mater Today Bio 13 (2022 Feb 9) 100216, https://doi.org/10.1016/j.mtbio.2022.100216. PMID: 35243291; PMCID: PMC8857474.
[38] L.Y. Long, C. Hu, W. Liu, C. Wu, L. Lu, L. Yang, Y.B. Wang, Microfibrillated cellulose-enhanced carboxymethyl chitosan/oxidized starch sponge for chronic diabetic wound repair, Mater Sci Eng C Mater Biol Appl 135 (2022 Apr) 112669, https://doi.org/10.1016/j.msec.2022.112669. Epub 2022 Jan 24. PMID: 35581075.
[39] B. Guo, R. Dong, Y. Liang, M. Li, Haemostatic materials for wound healing applications, Nat. Rev. Chem 5 (11) (2021 Nov) 773–791, https://doi.org/10.1038/s41570-021-00323-z. Epub 2021 Sep 17. PMID: 37117664.
[40] Y. Guo, M. Wang, Q. Liu, G. Liu, S. Wang, J. Li, Recent advances in the medical applications of hemostatic materials, Theranostics 13 (1) (2023 Jan 1) 161–196, https://doi.org/10.7150/thno.79639. PMID: 36593953; PMCID: PMC9800728.
[41] L. Mu, L. Qi, H. Long, J. Huang, Z. Zhong, X. Shi, C. Chen, Q. Ye, Photothermal fibrous chitosan/polydopamine sponge for intraoperative hemostasis and prevention of tumor recurrence in hepatocellular carcinoma resection, Adv. Sci. (Weinh.) 11 (3) (2024 Jan) e2304053, https://doi.org/10.1002/advs.202304053. Epub 2023 Nov 29. PMID: 38029340; PMCID: PMC10797464.
[42] Z. Yu, X. Fu, T. Lucas, H. Zhao, C. Chen, I. Dubail, Y. Chen, G. Patriarche, J. Gateau, F. Gazeau, A. Jamet, M. Lepoitevin, C. Serre, MOF-enhanced phototherapeutic wound dressings against drug-resistant bacteria, Adv. Healthcare Mater. 14 (1) (2025 Jan) e2402418, https://doi.org/10.1002/adhm.202402418. Epub 2024 Oct 26. PMID: 39460484; PMCID: PMC11694089.
[43] Y. Chen, B. Gu, X. Hao, Z. Lu, D. Wang, Nanofibrous membrane/thermoresponsive hydrogel composites with temperature-controlled capability for enhancing infected wounds healing, J. Colloid Interface Sci. 680 (Pt A) (2025 Feb 15) 172–180, https://doi.org/10.1016/j.jcis.2024.10.170. Epub 2024 Oct 28. PMID: 39504747.
[44] J. Wang, J. Lin, L. Chen, L. Deng, W. Cui, Endogenous electric-field-coupled electrospun short fiber via collecting wound exudation, Adv. Mater. 34 (9) (2022 Mar) e2108325, https://doi.org/10.1002/adma.202108325. Epub 2022 Jan 15. PMID: 34902192.
[45] Z. Jiang, L. Chen, L. Huang, S. Yu, J. Lin, M. Li, Y. Gao, L. Yang, Bioactive materials that promote the homing of endogenous mesenchymal stem cells to improve wound healing, Int J Nanomedicine 19 (2024 Jul 30) 7751–7773, https://doi.org/10.2147/IJN.S455469. PMID: 39099796; PMCID: PMC11297574.
[46] J. Dong, W. Wang, W. Zhou, S. Zhang, M. Li, N. Li, G. Pan, X. Zhang, J. Bai, C. Zhu, Immunomodulatory biomaterials for implant-associated infections: from conventional to advanced therapeutic strategies, Biomater. Res. 26 (1) (2022 Dec 5) 72, https://doi.org/10.1186/s40824-022-00326-x. PMID: 36471454; PMCID: PMC9721013.
[47] W. Zhang, K. Zha, W. Hu, Y. Xiong, S. Knoedler, D. Obed, A.C. Panayi, Z. Lin, F. Cao, B. Mi, G. Liu, Multifunctional hydrogels: advanced therapeutic tools for osteochondral regeneration, Biomater. Res. 27 (1) (2023 Aug 4) 76, https://doi.org/10.1186/s40824-023-00411-9. PMID: 37542353; PMCID: PMC10403923.
[48] J. Lee, H.N. Choi, H.J. Cha, Y.J. Yang, Microporous hemostatic sponge based on silk fibroin and starch with increased structural retentivity for contact activation of the coagulation cascade, Biomacromolecules 24 (4) (2023 Apr 10) 1763–1773, https://doi.org/10.1021/acs.biomac.2c01512. Epub 2023 Mar 23. PMID: 36951240.
[49] X.F. Wang, M.L. Li, Q.Q. Fang, W.Y. Zhao, D. Lou, Y.Y. Hu, J. Chen, X.Z. Wang, W. Q. Tan, Flexible electrical stimulation device with Chitosan-Vaseline® dressing accelerates wound healing in diabetes, Bioact. Mater. 6 (1) (2020 Aug 19) 230–243, https://doi.org/10.1016/j.bioactmat.2020.08.003. PMID: 32913931; PMCID: PMC7451868.